
Article:
Ashall, C., Hoeflich, P., Baron, E. et al. (2024) A JWST medium-resolution MIRI spectrum and models of the type Ia supernova 2021aefx at +415 days. The Astrophysical Journal, 975 (2). 203. ISSN: 0004-637X

https://doi.org/10.3847/1538-4357/ad6608

The Astrophysical Journal, 975:203 (30pp), 2024 November 10 https://doi.org/10.3847/1538-4357/ad6608

A JWST Medium-resolution MIRI Spectrum and Models of the Type Ia Supernova 2021aefx at +415 days

C. Ashall[1,2], P. Hoeflich[3], E. Baron[4,5], M. Shahbandeh[6], J. M. DerKacy[1], K. Medler[1], B. J. Shappee[7], M. A. Tucker[8,33], E. Fereidouni[3], T. Mera[3], J. Andrews[9], D. Baade[10], K. A. Bostroem[11,34], P. J. Brown[12], C. R. Burns[13], A. Burrow[14], A. Cikota[15], T. de Jaeger[16], A. Do[17], Y. Dong[18], I. Dominguez[19], O. Fox[6], L. Galbany[20,21], E. Y. Hsiao[3], K. Krisciunas[12], B. Khaghani[1], S. Kumar[22], J. Lu[23], J. R. Maund[24], P. Mazzali[25,26], N. Morrell[27], F. Patat[10], C. Pfeffer[1], M. M. Phillips[27], J. Schmidt[28], S. Stangl[14], C. P. Stevens[1], M. D. Stritzinger[29], N. B. Suntzeff[12], C. M. Telesco[30], L. Wang[31], and Y. Yang[32,35]

[1] Department of Physics, Virginia Tech, Blacksburg, VA 24061, USA; chris.ashall24@gmail.com
[2] Institute for Astronomy, University of Hawai'i, 2680 Woodlawn Drive, Honolulu HI 96822, USA
[3] Department of Physics, Florida State University, 77 Chieftan Way, Tallahassee, FL 32306, USA
[4] Planetary Science Institute, 1700 East Fort Lowell Road, Suite 106, Tucson, AZ 85719-2395, USA
[5] Hamburger Sternwarte, Gojenbergsweg 112, D-21029 Hamburg, Germany
[6] Space Telescope Science Institute, 3700 San Martin Drive, Baltimore, MD 21218-2410, USA
[7] Institute for Astronomy, University of Hawai'i at Manoa, 2680 Woodlawn Drive, Honolulu, HI 96822, USA
[8] Center for Cosmology and AstroParticle Physics, The Ohio State University, 191 West Woodruff Avenue, Columbus, OH 43210, USA
[9] Gemini Observatory/NSF's NOIRLab, 670 North A'ohoku Place, Hilo, HI 96720-2700, USA
[10] European Organization for Astronomical Research in the Southern Hemisphere (ESO), Karl-Schwarzschild-Str. 2, 85748 Garching b. München, Germany
[11] Steward Observatory, University of Arizona, 933 North Cherry Avenue, Tucson, AZ 85721-0065, USA
[12] George P. and Cynthia Woods Mitchell Institute for Fundamental Physics and Astronomy, Texas A&M University, Department of Physics and Astronomy, College Station, TX 77843, USA
[13] Observatories of the Carnegie Institution for Science, 813 Santa Barbara Street, Pasadena, CA 91101, USA
[14] Homer L. Dodge Department of Physics and Astronomy, University of Oklahoma, 440 West Brooks, Room 100, Norman, OK 73019-2061, USA
[15] Gemini Observatory/NSF's NOIRLab, Casilla 603, La Serena, Chile
[16] Sorbonne Université, CNRS/IN2P3, LPNHE, F-75005, Paris, France
[17] Institute of Astronomy and Kavli Institute for Cosmology, Madingley Road, Cambridge, CB3 0HA, UK
[18] Department of Physics, University of California, 1 Shields Avenue, Davis, CA 95616-5270, USA
[19] Universidad de Granada, 18071, Granada, Spain
[20] Institute of Space Sciences (ICE, CSIC), Campus UAB, Carrer de Can Magrans, s/n, E-08193 Barcelona, Spain
[21] Institut d'Estudis Espacials de Catalunya (IEEC), E-08034 Barcelona, Spain
[22] Department of Astronomy, University of Virginia, 530 McCormick Road, Charlottesville, VA 22904, USA
[23] Department of Physics and Astronomy, Michigan State University, East Lansing, MI 48824, USA
[24] Department of Physics and Astronomy, University of Sheffield, Hicks Building, Hounsfield Road, Sheffield S3 7RH, UK
[25] Astrophysics Research Institute, Liverpool John Moores University, UK
[26] Max-Planck Institute for Astrophysics, Garching, Germany
[27] Las Campanas Observatory, Carnegie Observatories, Casilla 601, La Serena, Chile
[28] Citizen Scientist
[29] Department of Physics and Astronomy, Aarhus University, Ny Munkegade 120, DK-8000 Aarhus C, Denmark
[30] Department of Astronomy, University of Florida, Gainesville, FL 32611, USA
[31] Department of Physics and Astronomy, Texas A&M University, College Station, TX 77843, USA
[32] Department of Astronomy, University of California, Berkeley, CA 94720-3411, USA
Received 2024 April 25; revised 2024 June 27; accepted 2024 June 29; published 2024 November 4

Abstract

We present a JWST MIRI medium-resolution spectrometer spectrum (5–27 μm) of the Type Ia supernova (SN Ia) SN 2021aefx at +415 days past *B*-band maximum. The spectrum, which was obtained during the iron-dominated nebular phase, has been analyzed in combination with previous JWST observations of SN 2021aefx to provide the first JWST time series analysis of an SN Ia. We find that the temporal evolution of the [Co III] 11.888 μm feature directly traces the decay of ^{56}Co. The spectra, line profiles, and their evolution are analyzed with off-center delayed-detonation models. Best fits were obtained with white dwarf (WD) central densities of $\rho_c = 0.9{-}1.1 \times 10^9$ g cm^{-3}, a WD mass of $M_{\rm WD} = 1.33{-}1.35\,M_\odot$, a WD magnetic field of $\approx 10^6$ G, and an off-center deflagration-to-detonation transition at $\approx 0.5\,M_\odot$ seen opposite to the line of sight of the observer (−30°). The inner electron capture core is dominated by energy deposition from γ-rays, whereas a broader region is dominated by positron deposition, placing SN 2021aefx at +415 days in the transitional phase of the evolution to the positron-dominated regime. The formerly "flat-tilted" profile at 9 μm now has a significant contribution from [Ni IV], [Fe II], and [Fe III] and less from [Ar III], which alters the shape of the feature as positrons mostly excite the

[33] CCAPP Fellow.
[34] LSSTC Catalyst Fellow.
[35] Bengier-Winslow-Robertson Postdoctoral Fellow.

low-velocity Ar. Overall, the strength of the stable Ni features in the spectrum is dominated by positron transport rather than the Ni mass. Based on multidimensional models, our analysis is consistent with a single-spot, close-to-central ignition with an indication of a preexisting turbulent velocity field and excludes a multiple-spot, off-center ignition.

Unified Astronomy Thesaurus concepts: Type Ia supernovae (1728); Supernovae (1668)

Materials only available in the online version of record: data behind figure

1. Introduction

Type Ia supernovae (SNe Ia) originate from the thermonuclear disruption of a carbon–oxygen (C–O) white dwarf (WD) in a multiple-star system (Hoyle & Fowler 1960), yet to date, the exact details of their progenitor scenarios or explosion mechanisms are unknown. Determining the exact origin of SNe Ia is essential if we are to understand the nucleosynthesis of heavy elements and improve the use of SNe Ia as extragalactic distance indicators (see Riess 2017 and Seitenzahl & Townsley 2017 for recent reviews).

Potential SN Ia progenitor scenarios include (1) the single degenerate (SD) scenario, which consists of a C–O WD and a nondegenerate companion star (Whelan & Iben 1973); (2) the double degenerate (DD) scenario, which consists of two WDs (Iben & Tutukov 1984; Webbink 1984); and (3) a triple/quadruple system consisting of at least two C–O WDs (Thompson 2011; Pejcha et al. 2013). There is also a complex interplay between the progenitor scenario and the explosion mechanism, where many explosion mechanisms can theoretically occur within each progenitor scenario. Two of the leading explosion mechanisms include the explosion of a near-Chandrasekhar-mass ($M_{\rm Ch}$) WD (Iben & Tutukov 1984; Khokhlov 1991) and the detonation of a sub-$M_{\rm Ch}$ WD (Livne & Arnett 1995). Both of these can occur in SD and DD systems. In the near-$M_{\rm Ch}$ explosion, the WD accretes H, He, or C material from a nondegenerate or degenerate companion star until it approaches the $M_{\rm Ch}$, during which time densities in the center of the star become high enough for a simmering stage to occur and a thermonuclear disruption begins (Khokhlov 1991). The flame can propagate as a deflagration, detonation, or both via a deflagration-to-detonation transition (DDT; Khokhlov 1991; Hoeflich et al. 1995; Gamezo et al. 2003; Poludnenko et al. 2019). In the sub-$M_{\rm Ch}$ scenario, a surface He layer detonates and produces an inward shock wave that disrupts the whole WD. This can occur for a variety of core (0.6–1.1 $M_{\odot}$) and He shell (0.01–0.2 $M_{\odot}$) masses, although only the higher-mass WDs and smaller He shell masses are expected to reproduce the observed properties of SNe Ia (Livne & Arnett 1995; Shen et al. 2018; Boos et al. 2021).

Observations of SNe Ia during the nebular phase reveal their inner layers. Spectra at these epochs can be used to measure the high-density burning regions in the ejecta (e.g., Axelrod 1980; Mazzali et al. 2007, 2020; Ashall et al. 2016; Maguire et al. 2018; Jerkstrand et al. 2020; Hoeflich et al. 2021; Kumar et al. 2023). A spectral region of particular interest is at mid-infrared (MIR) wavelengths (~5–27 μm), as it contains lines from critical ions that do not have suitable transitions in the optical or near-infrared (NIR). These ions can be used to distinguish between the leading progenitor and explosion scenarios. Prior to the launch of the James Webb Space Telescope (JWST), there were four SNe Ia that had MIR ($\lambda > 5$ μm) spectral observations, and there were seven published MIR spectra of SNe Ia in total (see the introduction of DerKacy et al. 2023a for more details). These data provided new insights into SN Ia explosions, but the interpretation was hampered by a low signal-to-noise ratio (S/N) and low spectral resolution.

The launch of JWST has opened up a new era of transient astronomy. To date, JWST spectra of three nearby SNe Ia have been published. These are SN 2022xkq (DerKacy et al. 2024a), SN 2022pul (Kwok et al. 2024; Siebert et al. 2024), and SN 2021aefx (DerKacy et al. 2023a; Kwok et al. 2023). Of these, SN 2021aefx is the best-observed SN Ia. Broadband NIR +MIR JWST imaging was obtained at +255 days after B-band maximum, which enabled the late-time NIR+MIR decline rates and MIR flux contribution in the explosion to be determined (Mayker Chen et al. 2023). Spectra of SN 2021aefx were acquired at +255 days (Kwok et al. 2023) and +323 days (DerKacy et al. 2023a) past B-band maximum. These spectra revealed many unique features including multiple stable Ni lines, which are indicative of high-density burning, a "flat-tilted" [Ar III] 8.991 μm profile, and a strong [Co III] 11.888 μm resonance feature (DerKacy et al. 2023a; Kwok et al. 2023). Spectral modeling of the JWST data indicated that SN 2021aefx is consistent with a delayed-detonation near-$M_{\rm Ch}$ explosion of a C–O WD that had an off-center DDT and produced 5.9×10^{-2} $M_{\odot}$ of ^{58}Ni (DerKacy et al. 2023a; although see Blondin et al. 2023). However, all of the previous spectra of SN 2021aefx were obtained with the low-resolution spectral mode and at wavelengths less than 14 μm. The medium-resolution spectrometer (MRS) on the Mid-Infrared Instrument (MIRI) has a resolving power of ~2700 and wavelength coverage from ~5 to 27 μm and is therefore ideal for obtaining precision velocity measurements as well as observations at long wavelengths.

Here we present the first observed JWST MIRI/MRS spectrum of a SN Ia.[36] In Section 2, we discuss the observations and data reduction. In Section 3, we present line identification, followed by spectral comparisons in Section 4. In Section 5, we discuss the time series spectral evolution. In Section 6, we use self-consistent multidimensional models to produce synthetic spectra, where we demonstrate how the MIRI/MRS data can be used in conjunction with synthetic spectra and line profiles to understand the underlying explosion physics and the conditions at the thermonuclear runaway. A summary of our results and our conclusions are presented in Section 7.

2. Observations and Data Reduction

SN 2021aefx was discovered on 2021 November 11.3 (MJD = 59529.5) by the Distance Less Than 40 Mpc Survey (Tartaglia et al. 2018). It was located at $\alpha = 04^{\rm h}19^{\rm m}53\overset{\rm s}{.}40$, $\delta = -54°56'53\overset{''}{.}09$, southwest of the center of its host galaxy NCG 1566 ($z = 0.0050$). The location of SN 2021aefx in its host galaxy is shown in Figure 1. Early-time observations and

[36] The first published JWST MIRI/MRS spectra of a SN Ia was SN 2022xkq (DerKacy et al. 2024a).

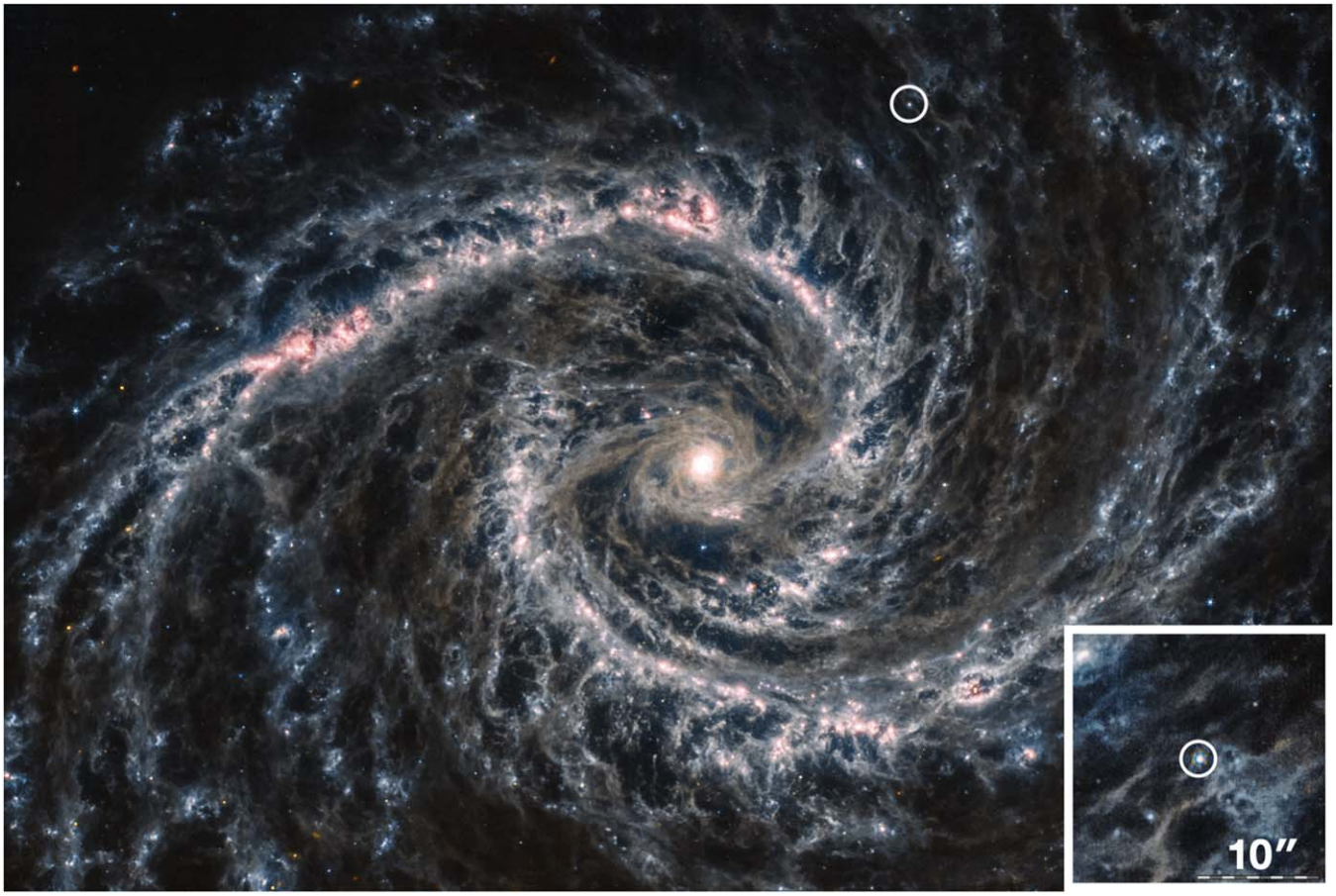

Figure 1. A stacked composite image of NGC 1566 with photometric data obtained with JWST's MIRI; individual bands are published in Chen et al. (2023). Here, SN 2021aefx is at a phase of +357 days past *B*-band maximum and is highlighted in the white circle. North is 1.°5 counterclockwise from left. An inset around the SN is shown in the bottom right corner. For the original image, see www.flickr.com/photos/geckzilla/52523099436/.

Table 1
Log of JWST Observations

Parameter	Value	Value	Value
	MIRI/MRS Spectra		
Subband	Short	Medium	Long
Groups per integration	35	35	36
Integrations per exp.	3	3	3
Exposures per dither	1	1	1
Total dithers	12	12	12
Exp. time (s)	10,224.88	10,224.88	10,511.565
Readout pattern	SLOWR1	SLOWR1	SLOWR1

Note. The spectrum was taken at MJD = 59964.34, which is rest-frame +415 days relative to *B*-band maximum.

Table 2
Synthetic Photometry Produced from the +415 Day Spectrum of SN 2021aefx

Filter	Flux (mJy)
F770W	0.1724
F1000W	0.3931
F1130W	0.3412
F1280W	0.1330
F1500W	0.1165

analysis of SN 2021aefx indicated that it was discovered within hours of the explosion and had an early excess emission in the *u* band, a quickly evolving color curve, and extremely high spectral velocities (Ashall et al. 2022; Hosseinzadeh et al. 2022; Ni et al. 2023). By maximum light, it resembled a normal-luminosity SN Ia, demonstrating that SN 2021aefx is only unusual in the outermost layers (Ashall et al. 2022; Hosseinzadeh et al. 2022; Ni et al. 2023).

JWST MIRI/MRS spectral observations of SN 2021aefx were triggered through JWST-GO-2114 (Ashall et al. 2021). Observations began on 2023 January 20 at 03:34:38 (MJD = 59964.15) and ended on 2023 January 20 at 12:47:50 (MJD = 59964.53). We take our time of observation as the midpoint, MJD = 59964.34. Throughout this work, we use a time of *B*-band maximum of MJD = 59547.25 (DerKacy et al. 2023a), implying that the spectrum was obtained at rest-frame +415 days past *B*-band maximum light.

Spectral data were acquired using the MRS on MIRI with the short, medium, and long gratings and with each channel to produce a continuous spectrum from ∼5 to 27 μm. The details of the instrument setup can be found in Table 1. The total exposure time was 8.6 hr.

The data were reduced using a custom-built pipeline designed to extract observations of faint point sources that have complex backgrounds in MIRI/MRS data cubes (see Shahbandeh et al. 2024). The details of the data reduction can be found in

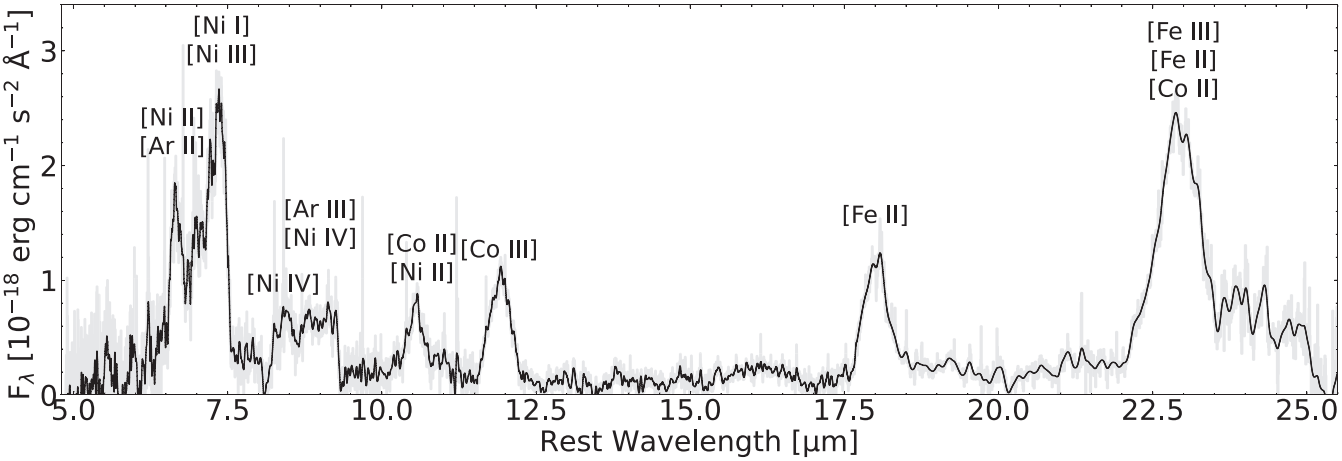

Figure 2. The MIRI/MRS spectrum of SN 2021aefx at +415 days past maximum light. The raw data are plotted in light gray behind. Due to the fact that the spectrum is heavily oversampled, it has been smoothed to the instrumental resolution (black). The dominant ions that contribute to each feature are labeled. The raw spectrum is available.

(The data used to create this figure are available in the online article.)

Appendix A. This data reduction technique dramatically reduced the background flux level by 2 orders of magnitude across all channels. This both increases the S/N in the extraction of the SN and ensures that the continuum is dominated by the SN and not instrumental flux.

The final spectrum has been smoothed with Spextractor (Burrow et al. 2020) channel by channel to properly account for the differences in resolution across the full MIRI/MRS wavelength coverage. Throughout this work, the spectra were corrected to rest frame using the recessional velocity of 1500 km s^{-1} and a rotational galactic velocity of 65 ±60 km s^{-1} at the location of the SN (Elagali et al. 2019).

Comparing the MIRI low-resolution spectrometer (LRS) and MIRI/MRS spectra of SN 2021aefx is useful for checking both the flux and wavelength calibration. It is known from the comparison between JWST MIRI photometry and JWST MIRI/LRS spectra that the absolute flux calibration of the MIRI/LRS data of SN 2021aefx is within 2% (Kwok et al. 2023; Chen et al. 2023). Generally, for MIRI/MRS data, it is thought that the flux calibration is accurate to 5.6% ± 0.7% (Argyriou et al. 2023). This was also confirmed using MIRI/MRS data of SN 2022acko, where the spectral flux in channels 1, 2, and 3 was found to be consistent with simultaneous MIRI broadband photometry (Shahbandeh et al. 2024). However, it is not yet known how well the pipeline extracts the SN flux in channel 4 and how successful it is at accurately removing the background from both the instrument and the underlying host galaxy. Overall, the flux of the SN 2021aefx MIRI/MRS spectrum at +415 days is lower than that at the previous epoch (see Section 5). It is also apparent that the decrease in peak flux is more rapid at earlier epochs compared to later ones. This is consistent with the light curve flattening with time. Although there is no simultaneous photometry at +415 days, this time series behavior suggests that the flux calibration of the MIRI/MRS spectrum is accurate. However, for future literature comparison, we provide synthetic photometry using the JWST passbands; see Table 2. Finally, we note that the wavelength calibration of the MIRI/MRS spectra is accurate to within 9 km s^{-1} at 5 μm and to 27 km s^{-1} at 28 μm (Argyriou et al. 2023).

3. Line Identifications

The fully stitched four-channel MIRI/MRS spectrum is presented in Figure 2. The strongest lines that contribute to the formation of the spectral features have been labeled. These line identifications are based on radiation hydrodynamical models discussed in Section 6. At short wavelengths (<14 μm), the line IDs are consistent with those presented in DerKacy et al. (2023a) and Kwok et al. (2023). However, the individual line strengths and profiles have evolved over the intervening 92 days between observations, demonstrating that the physical processes driving the spectral formation have profoundly changed (see Section 6).

We identify four dominant regions of line formation, which are presented in Figure 3. The strongest lines contributing to each spectral region are described below. For the line identification, we use the models presented in Section 6.

Between 5 and 7.5 μm, the spectrum is dominated by stable Ni lines, including [Ni I] 5.893 μm and [Ni II] 6.636 and 6.920 μm, as well as [Fe II] 5.674 μm and [Ar II] 6.985 μm. Between 7.5 and 10.0 μm, lines of [Ni IV] 8.405, 8.945 μm and [Ar III] 8.991 μm are the strongest.

In the wavelength range of 10.0–15.0 μm, the strongest features are [Fe II] 10.189, 12.286, and 12.642 μm; [Ni II] 10.682 and 12.729 μm; [Ni IV] 11.13 μm; [Ni I] 12.001 μm; [Co III] 11.888 μm; and [Co I] 12.255 μm.

Between 15 and 20 μm, the strongest spectral lines contributing to the formation of the features are [Fe II] 17.936 and 19.056 μm and [S III] 18.713 μm. Beyond 20 μm, the spectrum is dominated by [Fe III] 22.925 μm, [Fe I] 24.052 μm, [Co III] 24.070 μm, and [Fe II] 24.519 and 25.988 μm.

It should be noted that the line IDs beyond 20 μm are tentative, as the background subtraction is uncertain at these wavelengths. Furthermore, the flux calibration at these wavelengths is highly uncertain, and the spectrum at wavelengths >25 μm should not be trusted until a more accurate reduction in channel 4 is available. Furthermore, it is not possible to confidently identify all spectral features, as data for many atomic line transitions in these MIR regions are missing. However, through spectral modeling, we can identify some of the unknown line strengths as well as estimates of the

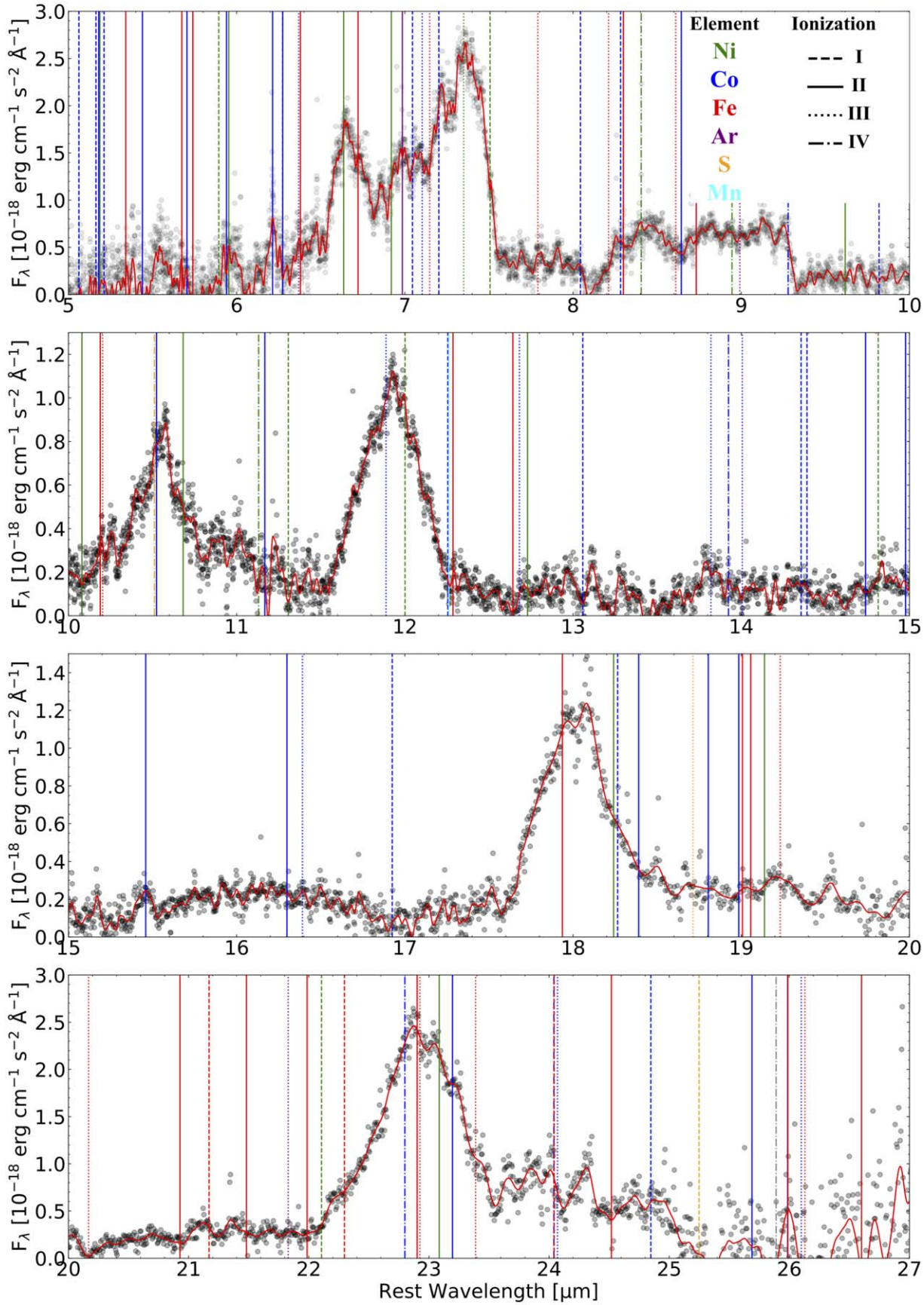

Figure 3. The +415 day spectrum of SN 2021aefx with the main contributing ions labeled.

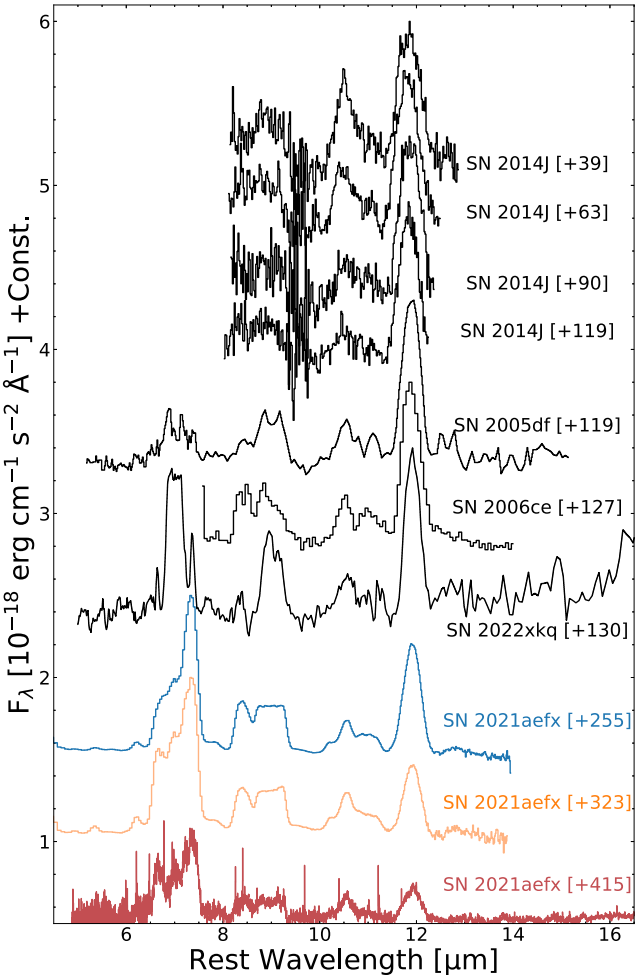

Figure 4. A selection of MIR SN Ia spectra. Times relative to *B*-band maximum are provided next to each observation. All SNe Ia in this plot are normal SNe Ia except for SN 2022xkq, which is subluminous.

flux contribution from the weaker lines (see Section 6.3.1 and Appendix E).

4. Spectral Comparison

Figure 4 shows a spectral comparison plot between SN 2021aefx and a sample of published MIR SN Ia observations. The previous sample covers the evolution of SNe Ia from +39 to +323 days past *B*-band maximum. All previous MIRI/LRS spectral observations of SN 2021aefx were rereduced using the method outlined in DerKacy et al. (2023a) but using pipeline version 1.13.4 and CRDS version 1223.pmap. Overall, the line profiles and strengths are unaffected by the new reduction, but this version of the pipeline and calibration files fixes previously known issues with the MIRI/LRS wavelength calibration.

All spectra share similarities and consist of broad emission features that are composed of forbidden line transitions from Ar, Co, Fe, and Ni. The strongest of these is the [Co III] 11.888 μm resonance feature. However, the capabilities and power of JWST become apparent with the first two spectra of SN 2021aefx. These spectra were observed using MIRI/LRS ($R \sim 100$) and revealed many spectral features that had not been observed before. In particular, a "flat-tilted" [Ar III] 8.991 μm profile and multiple ionization states of Ni were observed (DerKacy et al. 2023a; Kwok et al. 2023). The MIRI/MRS spectrum presented in this work is dominated by similar spectral features as earlier epochs, although with the higher resolution ($R \sim 2700$), we can more accurately determine the exact region of the ejecta in which these ions are located as well as examine the data for resolved features. Overall, the MIRI/MRS data allow for detailed line IDs and analysis of ejecta structure at a level not possible with MIRI/LRS data; see Figure 5.

To date, the spectrum of SN 2022xkq at 130 days past maximum light is the only published MIRI/MRS spectrum of an SN Ia (DerKacy et al. 2024a). The top panel of Figure 6 shows a comparison between the low-luminosity SN 2022xkq and the normal-luminosity SN 2021aefx. Although they are taken 285 days apart, many of the same ions form the spectrum but with different strengths and ratios, reflecting the variations in ionization balances due to phase and subtype differences. In SN 2021aefx, the stable Ni features are stronger than those in SN 2022xkq relative to both the Ar and Co features. There is also a significant contribution from Fe in the spectral formation of SN 2021aefx, which is prevalent in these epochs due to the decay of ^{56}Co. The spectra of SN 2021aefx and SN 2022xkq also vary in the ionization state of Ar, where for the low-luminosity SN 2022xkq, [Ar II] is the dominant ionization state, but for the normal-luminosity SN 2021aefx, [Ar III] is the dominant ionization state of Ar. For SN 2021aefx, the Ar features have significantly more line blending from Fe-group elements than in SN 2022xkq.

5. Temporal Evolution of SN 2021aefx

The time evolution of the JWST MIR spectra of SN 2021aefx from +215 to +415 days relative to rest-frame *B*-band maximum light in absolute flux is presented in the bottom panel of Figure 6. As the data of SN 2021aefx are the first MIR time series of an SN from JWST, they allow us to follow the evolution of features as a function of time. We start by analyzing the [Co III] 11.888 μm feature, as it is the most prominent feature in the MIR spectra, and then proceed to the evolution of other dominant lines.

5.1. [Co III] 11.888 μm

The [Co III] 11.888 μm feature gets weaker as a function of time (see the top left panel of Figure 7). We quantitatively examine the evolution of this feature. For simplicity, we assume the feature can be modeled by a single Gaussian function, although there is likely some blending with the [Ni I] 12.001 μm line.

The peak velocity ($v_{\rm peak}$) of the [Co III] feature is $\sim$500 km s^{-1} at +255 days and +323 days and increases to $\sim$750 km s^{-1} by +415 days. The values in $v_{\rm peak}$ are consistent between the MIRI/LRS and MIRI/MRS data once the error due to the low spectral resolution of the LRS data is considered.

The measured FWHM of the [Co III] 11.888 μm feature increases from $\sim$11,100 km s^{-1} at +255 days to $\sim$11,700 km s^{-1} at +415 days. The cause of this is likely driven by the strength of the [Co III] 11.888 μm line decreasing as a function of time and the [Ni I] 12.001 μm line getting stronger.

The peak flux of the [Co III] feature decreases from $\sim 4.2 \times 10^{-18}$ erg cm^{-1} s^{-2} Å^{-1} at +255 days to $\sim 1 \times 10^{-18}$ erg cm^{-1} s^{-2} Å^{-1} at +415 days. The evolution of the feature is well described by an exponential decay with a half-life of 76.72 ± 4.61 days. This is consistent with the half-life of

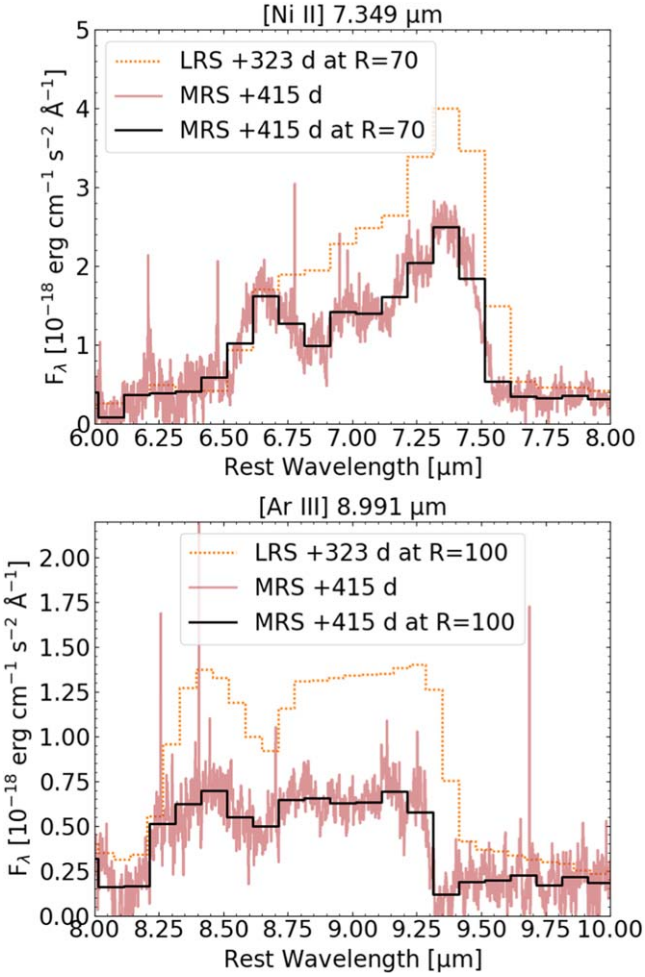

Figure 5. The MIRI/MRS data have been resampled to the spectral resolution of the MIRI/LRS data. For the [Ni II] 7.349 μm profile (top panel), many of the isolated features cannot be resolved in the MIRI/LRS resolution but are visible in the MIRI/MRS spectrum. For the [Ar III] 8.991 μm feature (bottom panel), the shape of the profile goes from "flat-tilted" to "flat-topped" between +323 and +415 days, demonstrating that the shape change is not caused by a resolution effect and is consistent with the physical interpretation provided in Section 6. We also note here that all MIRI/LRS data are heavily oversampled and should be resampled to the spectral resolution, as we have done in these panels, before direct comparison to the MIRI/MRS data.

^{56}Co, which is 77.27 days, demonstrating that the time evolution of this feature can be used to directly trace the energy deposition of the ^{56}Co in the ejecta. This trend is not found in the optical [Co III] feature at 6200 Å, which has been found to decrease faster than the ^{56}Co cooling rate (McClelland et al. 2013). This highlights the uniqueness of the [Co III] 11.888 μm feature. It is a resonance line, and all of the recombination passes though it. It also demonstrates that the [Co III] line dominates this feature throughout, as well as confirming that the flux calibration of the spectra is consistent between the MIRI/LRS and MIRI/MRS data. Continued observations of this feature in Cycles 2 and 3 (DerKacy et al. 2023b, 2024b) up to +1150 days past maximum light will probe the region where radioactive ^{57}Co may dominate the heating. If there is little mixing in the inner part of the ejecta, this ^{57}Co will be located in the central $\sim$1000 km s^{-1} (Hoeflich et al. 2021). This may cause the [Co III] feature to become stronger and narrower over time. Following the evolution of this feature with future spectral observations will allow for the distribution and strength of the ^{57}Co to be characterized.

5.2. The Evolution of Other Important Features

We now turn our attention to the temporal evolution of four other features. These are the [Ni II] 7.349 μm, [Ni IV] 8.405 μm, [Co III] 10.523 μm, and [Ar II] 8.991 μm regions. Due to the more complex structures and blends in these features, we choose to concentrate on the evolution of only the peak flux. Figure 8 shows the evolution of these features in velocity space, as well as their peak flux as a function of time.

In the earlier phases, the [Ni II] 7.349 μm feature appears to be dominated by one transition, but by day +323, a blue wing appears in the emission profile. In the MIRI/LRS data, this blue wing is blended with the main [Ni II] 7.349 μm feature; however, it is resolved in the MIRI/MRS data at +415 days and shows two distinct components with many smaller overlapping emission features in the bluest wavelengths. We identify this blue feature as [Co I] 7.202μm. It is clear through this comparison that MIRI/MRS data are required to fully resolve the profiles, but even with the higher resolution, the emission profiles are a complex blend of many lines, some of which are unknown. The peak flux of this wavelength region as a function of time does not follow the radioactive decay of ^{56}Co.

The [Ni IV] 8.405 μm feature appears to be dominated by one spectral ion throughout the MIRI/LRS time series of data. However, the MIRI/MRS data reveal that there are at least two resolved profiles contributing to this feature, one closer to the rest wavelength of [Ni IV] 8.405 μm and one at $\sim$9000 km s^{-1}. We identify the blue feature to be a blend of [Co I] 8.283 μm and [Fe II] 8.299 μm. The peak flux of this feature does decrease as a function of time, but unlike the [Co III] 11.888 μm feature, it does not follow the half-life of ^{56}Co.

The [Co III] 10.523 μm feature is the second-most-prominent [Co III] region in the MIR spectrum, and the shape of this profile changes dramatically between the MIRI/LRS and MIRI/MRS data. It is much narrower and peaked within the MIRI/MRS data. The evolution of the peak flux of this feature follows a half-life of 206.50 $\pm$ 22.79 days, which is more than twice that of what would be expected of ^{56}Co decay. This demonstrates the uniqueness of the [Co III] 11.888 μm feature, as it is both isolated and a resonance line, so all recombination passes through the transition. It also highlights that an apparently isolated feature, such as the [Co III] 10.523 μm, is still heavily blended and not dominated by a single transition, meaning that any velocity extracted from such features will be highly uncertain.

The [Ar II] 8.991 μm feature is unique, as it shows a flat-top profile. This flat-top profile (at earlier epochs, this was referred to as a "flat-tilted" profile) is seen throughout all of the spectra in the time series and has been interpreted as being caused by a shell of Ar in the ejecta (Kwok et al. 2023), which may come from an off-center DDT (DerKacy et al. 2023a). The blue side of this feature is clearly contaminated by emission from the [Ni IV] 8.405 μm transition. We also see that the peak of this feature does not follow the half-life of ^{56}Co. Overall, we stress that all of the line profiles shown in this section are highly blended, and only with improved atomic data can the true components that contribute to the MIRI/MRS spectrum of SN 2021aefx be extracted.

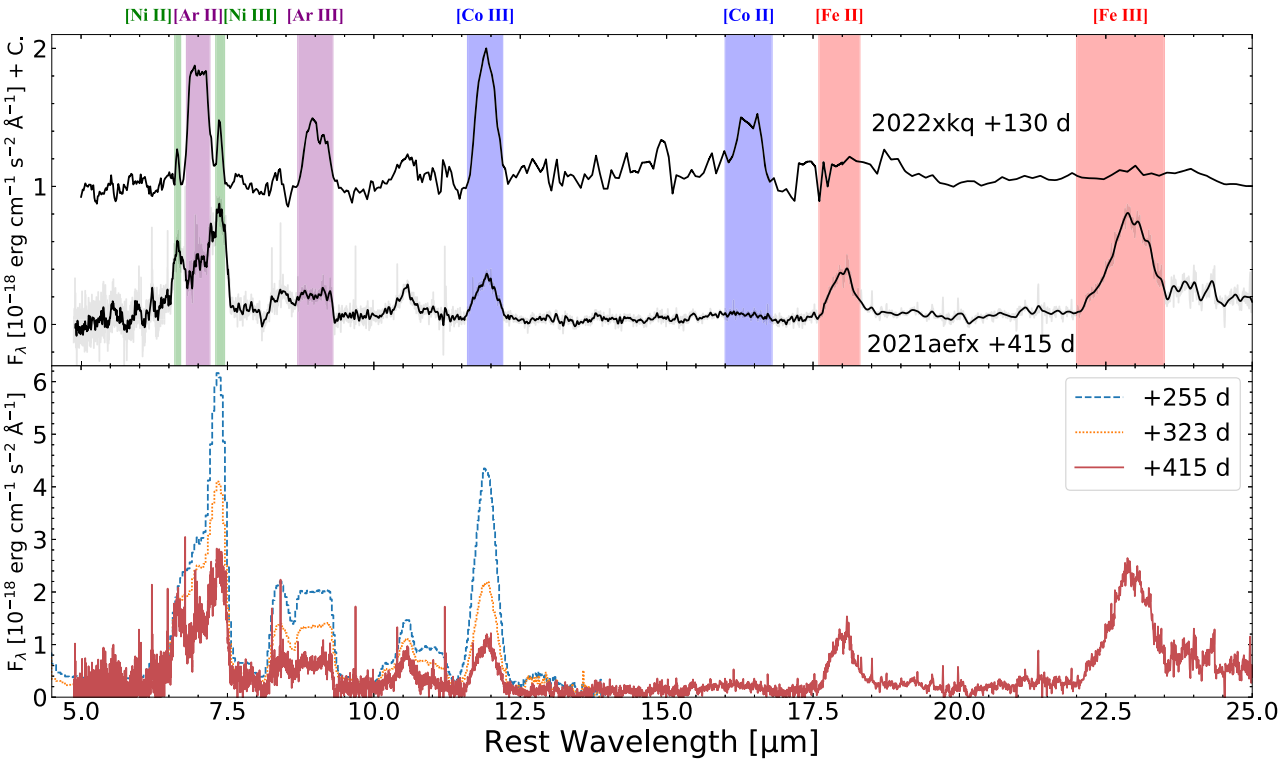

Figure 6. Top: a spectral comparison between the MIRI/MRS data of SN 2022xkq and SN 2021aefx. The dominant ions contributing to various spectral regions are highlighted with vertical colored bars. We note that SN 2022xkq is a low-luminosity SN Ia. Bottom: time series comparison of all published MIR spectra of SN 2021aefx.

5.3. *[Ni II]/[Co III] Ratio as a Function of Time*

Examining the peak flux ratio [Ni II] 7.349 μm/[Co III] 11.888 μm as a function of time is another useful measure. It allows us to determine how the temporal variation in the energy deposition, heating, and mixing between the ^{56}Ni region and the electron capture element region evolves. As can be seen in Figure 9, this ratio gradually increases throughout the time series. At later epochs, if the decay of ^{57}Co begins to dominate, it could be expected that this trend changes direction. However, this may heavily depend on the location of the ^{57}Co with relation to the stable Ni in the ejecta.

5.4. *Half-width at Half-maximum versus* v_{peak}

There are many overlapping spectral lines that contribute to the formation of the nebular phase spectrum of SN 2021aefx. MIRI/MRS observations allow for more of these lines to be resolved. However, many of the atomic line transitions and strengths are not known. Regardless of this, we attempt to fit the emission profiles of spectral features in order to get a broad understanding of where in the ejecta the emitting regions of certain ions are located. The full analysis is given in Appendix C. We stress that the lack of full line IDs and the assumption that all emitting line profiles can be explained by simple functions (where we inherently assume they are symmetrical) and the priors given in the fitting procedure make the results highly uncertain.

Figure 10 shows the half-width at half-maximum (HWHM) versus the peak velocity of ions that have been fit in Appendix C. Overall, we see no general trend with any of the ions. This is likely to be caused by the number of Gaussians required to reproduce the observed spectra, along with unknown spectral lines, and their corresponding strengths. Therefore, we emphasize that fitting spectra with multiple Gaussians has very little physical meaning, except in the case of isolated strong features such as the [Co III] 11.888 μm line. Hence, we turn our attention to the models below to further understand the physics and formation of the spectra. We also emphasize that both the high spectral resolution and the extended wavelength coverage of the MRS mode on MIRI are critical for the physical interpretation described below.

6. Models

In the following section, we compare the data to models. The simulations utilized in this work are computed using the HYDrodynamical RAdiation code (e.g., Höflich 2003a) that consists of physics-based modules that provide solutions for the rate equations that determine the nuclear reactions, the statistical equations needed to determine the atomic level populations, the equation of state, the matter opacities, the hydrodynamic evolution, and the radiation-transport equations (RTE). Here, the RTE is treated using variable Eddington tensor methods, with a Monte Carlo scheme providing the necessary closure relation to the momentum equations needed to solve the generalized scattering and non-LTE problem (Hoeflich 2002, 2017; Höflich 2003b; Penney & Hoeflich 2014; Diamond et al. 2015; Hristov et al. 2021). The relevant physics and current limitations of the simulations in the nebular phase are discussed in detail in Hoeflich et al. (2021). The growth of the WD mass toward $M_{\rm Ch}$ has been simulated following the approach by Sugimoto et al. (1979) and Nomoto (1982). The accretion rate and composition of the accreting material during the final stages have been tuned so that the ignition is triggered at a central density ρ_c (Hoeflich 2002; Diamond et al. 2015). To trigger a thermonuclear runaway at a ρ_c below $\approx$0.8–1.0 $\times$ 10^9 g cm^{-3} requires accretion rates in excess of

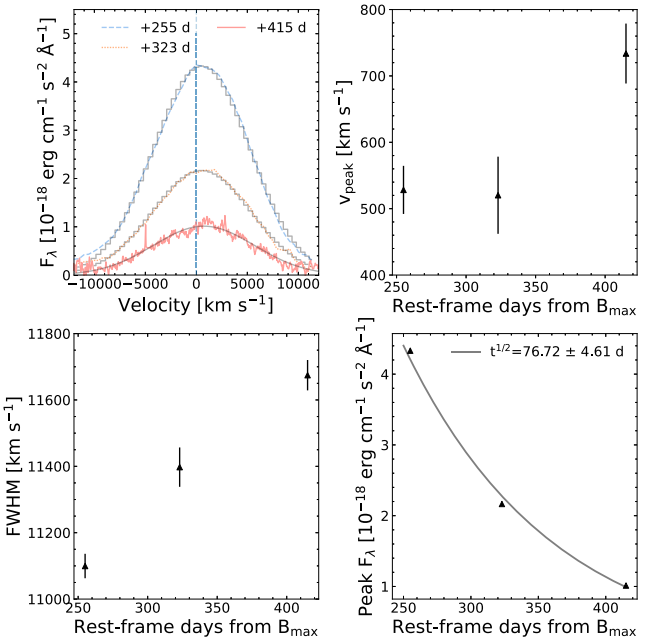

Figure 7. Top left: evolution of the [Co III] 11.888 μm feature as a function of time; for simplicity, it is fit with a single Gaussian profile. Top right: the velocity evolution of the peak of the emission profile. Bottom left: the evolution of the feature's FWHM. Bottom right: the peak flux of the feature as a function of time, along with a line of best fit with a decaying exponential function. For all panels, if the error bars are not visible, they are smaller than the markers. Furthermore, we have only plotted the fit error and not the resolution error.

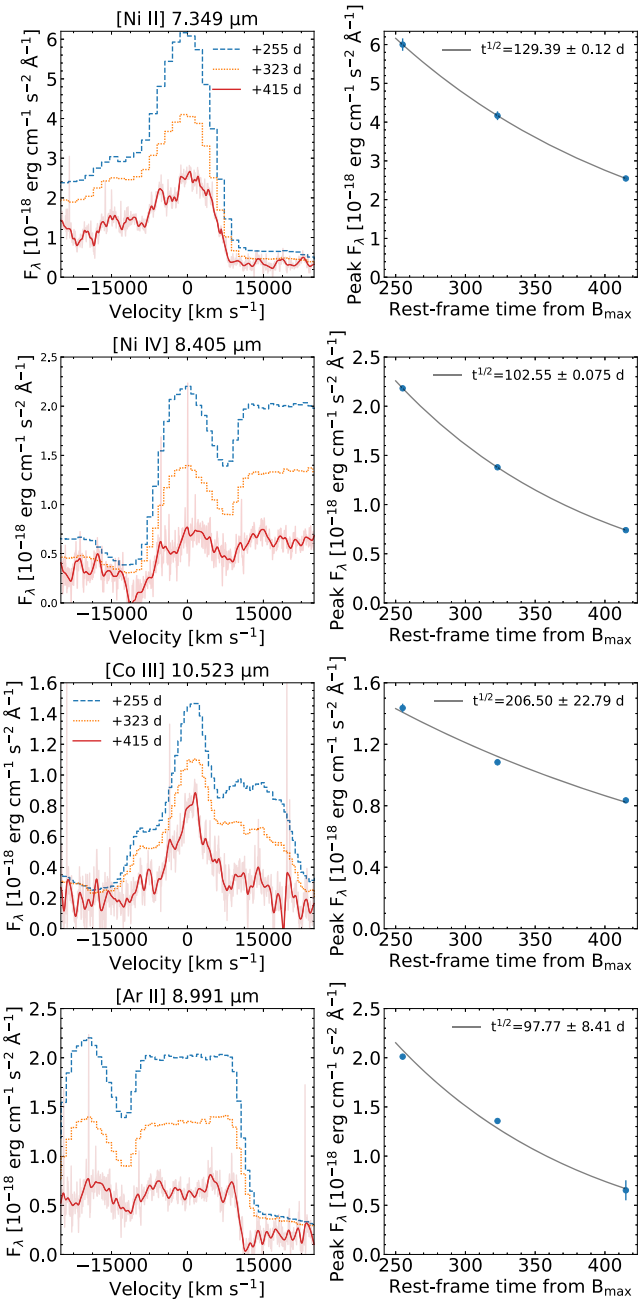

Figure 8. Left: the velocity profile evolution of four important wavelength ranges within MIR spectra of SN 2021aefx. For most regions, the MIRI/MRS data can resolve structure within features that appear blended in the MIRI/LRS mode; see also Figure 5. Right: the peak flux of the profiles as a function of time fit with exponential decay curves.

$2 \times 10^{-6}\, M_\odot\ \mathrm{yr}^{-1}$. To avoid over-Eddington luminosity of the accreting WD, He- or C-rich matter is required, at least during the final stages. This limit depends on the details of the physical processes that occur during the accretion, such as the Urca cooling by neutrinos (see Haensel 1995; Section 5.7 of Diamond et al. 2015). For a review of a wide variety of progenitor evolutions, see Alsabti & Murdin (2017 and references therein).

In this work, the explosion model is based on simulations of off-center delayed-detonation models following Livne (1999). This class of models has been successfully used to reproduce the photospheric and nebular phase flux and polarization spectra of SNe Ia. It has also been used to reproduce the abundance distributions in SN remnants and to study the role of SNe Ia as producers of the positrons observed in our Galaxy (Höflich et al. 2006; Penney & Hoeflich 2014; Fesen et al. 2015; Telesco et al. 2015; Hristov et al. 2021; Hoeflich et al. 2021; Mera Evans et al. 2022).

Here, the simulations are used with parameters that have been shown to reproduce the evolution of the polarization and flux spectra of the normal-luminosity SN 2019np (Hoeflich et al. 2023). These model parameters have been successfully applied to SN 2021aefx at +323 days if seen from $\Theta \approx -30^\circ$ (DerKacy et al. 2023a), where Θ is the angle between the equatorial plane defined by the orthogonal vector between the kinematic center and the location of the DDT. Note that a variety of Θ values have been found for different SNe using both line profiles and spectropolarimetry, e.g., SN 2003hv (Höflich et al. 2006; Motohara et al. 2006), SN 2003du (Höflich et al. 2004), SN 2012ke (Patat et al. 2012), SN 2019np (Hoeflich et al. 2023), and SN 2020qxp (Hoeflich et al. 2021). For nebular profiles of different SNe, the distribution of Θ is consistent with a random orientation relative to the observer. Line polarization during the photospheric phase favors angles close to the northern pole (i.e., Θ larger than 30°; Hoeflich et al. 2023). This can be understood by selective line absorption by a large-scale abundance asymmetry, as produced in an off-center DDT. Both effects combined support the notion of a loop-sided asymmetry. For objects with multiepoch observations, consistent values of Θ have been found, suggesting a large-scale abundance asymmetry. We note that the point of ignition and the DDT are distinct and are related to very different physical processes.

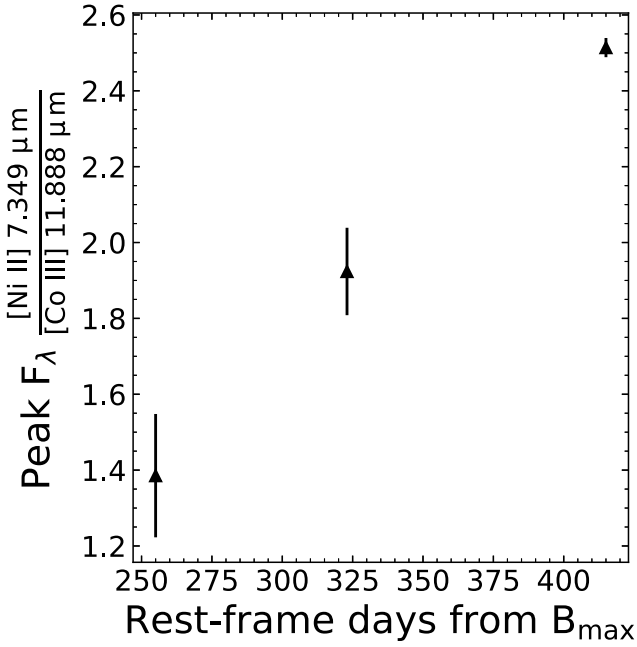

Figure 9. The ratio of the peak flux of the [Ni II] 7.349 μm–[Co III] 11.888 μm features as a function of time demonstrates that emission from stable Ni increasingly dominates the spectral formation. We chose to examine the peak flux here as it follows the bulk of the emission, and the features are too blended to obtain accurate values of HWHM.

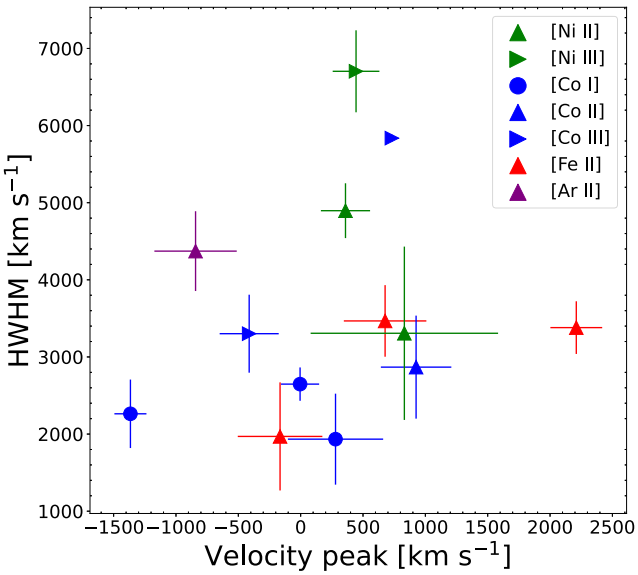

Figure 10. The peak velocity vs. HWHM of selected spectral features. As discussed in the text, these values are highly uncertain, and the detailed spectral modeling presented in Section 6 is needed to extract further information about the explosion.

In this work, the basic model parameters (the initial magnetic field of the WD, B, and the central density, ρ_c) have been extended to cover a larger range in values to take advantage of the increase in the spectral resolution of the MIRI/MRS data.

The model parameters are given in Table 3. The base model, model 25, serves as a reference to a series of simulations with various ρ_c; see Figure 11. To first order, the central density of the WD at the time of the runaway depends on the accretion rate and WD magnetic field. Note that the accretion on the WD is governed by the configuration of the progenitor, and the range of possible accretion depends on the composition of the accreted material (Sugimoto et al. 1979; Nomoto 1982). For comprehensive overviews, see the textbook by Alsabti & Murdin (2017). The WD masses of the models considered here are close to $M_{\rm Ch}$.

6.1. Resolution of Simulations

Medium-resolution spectra are crucial for accurately interpreting the physical characteristics of individual observed and synthetic features. For our discussion below, where we compare observations with theory, the spectral resolution sets the limit to resolve small features and their profiles. The spectral resolution of the data varies with wavelength, but $R \sim 2700$ corresponds to a velocity resolution of about $\sim$111 km s^{-1}. As in previous works (e.g., Hoeflich et al. 2023), the model domain is spatially resolved by an equidistant Cartesian grid of 300 points per dimension that covers an expansion velocity of $\approx$26,000 km s^{-1}. Taking into account the second-order discretization in spatial coordinates of the simulations, this translates into a spectral resolving power of $R \approx 600$. This corresponds to a velocity of $\approx$500 km s^{-1} for underlying physical features in the full-domain simulation. This resolution is employed for solving for the temperature structure and rate equations because optical depth effects in the UV are important for the ionization balance due to the incomplete Rosseland cycle (Hoeflich et al. 2021).[37]

For the emitted synthetic spectra and line profiles, more than 99.9% of the flux in the optical to MIR originates within 15,000 km s^{-1} because the energy is produced from the radioactive decay of ^{56}Ni/^{56}Co (see Figure 11). Therefore, the computed domain has been reduced to boost the resolving power to $R \approx 1200$, which corresponds to a velocity of $\approx$300 km s^{-1}. This allows for a direct comparison with the MIRI/MRS spectra without artificial convolution of the observed data. The model has approximately the same resolving power as the channel 4 data.

The typical scale over which the density and abundances vary in our models (see Figure 11) is $\approx$1000 km s^{-1}. Physically, smaller scales down to 100 km s^{-1} can be expected as a result of downward cascading in Rayleigh–Taylor instabilities in the outer layers. However, due to the large number of small plumes, a detection of density and chemical inhomogeneities requires an S/N better than 300 in the polarization spectra (Hoeflich et al. 2023) or in the peak flux of strong emission lines in flux spectra.

6.2. Energy Deposition and Ionization

The angle-averaged ionization structures at day +415 are shown in Figure 12. ^{56}Fe dominates the nuclear statistical equilibrium region through singly and doubly ionized species, as can be expected for normal-luminosity SNe Ia and underluminous SNe Ia at earlier times (Wilk et al. 2018; Shingles et al. 2020; Hoeflich et al. 2021). Because the density increases inward and the recombination rate depends on the square of the density, the ionization decreases toward the center. In the models, the ionization rate shifts toward more neutral ions compared to nebular calculation at $\approx$200–300 days (Wilk et al. 2018; Shingles et al. 2020; DerKacy et al. 2023a). At day +415, we see $\sim$5%–10% of neutral iron-group elements. One

[37] Even at 1000+ days, the UV optical depth remains large in the iron-rich region.

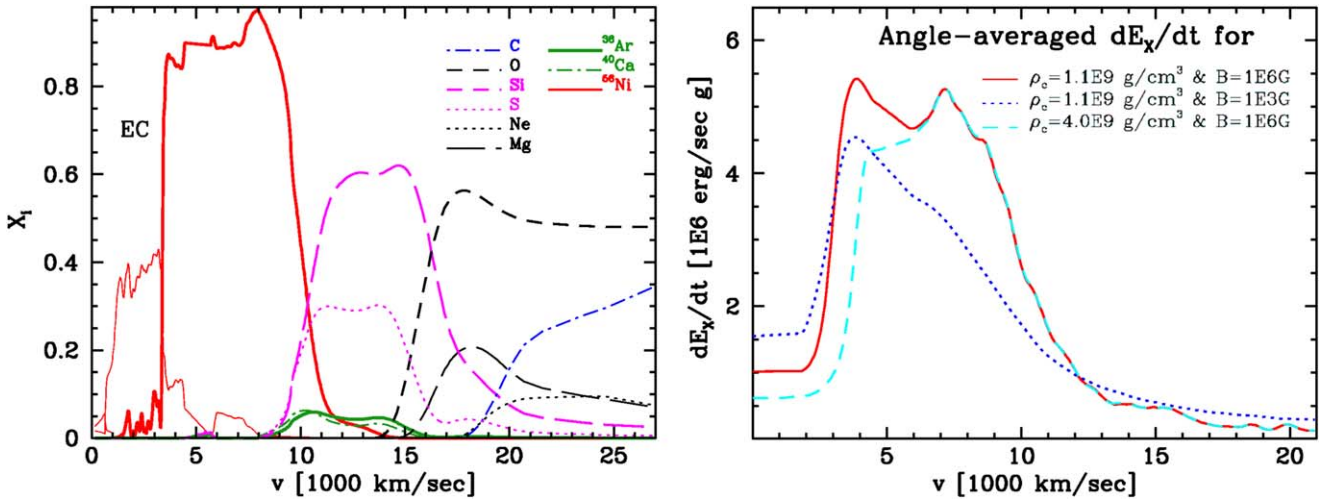

Figure 11. Left: the angle-averaged composition of our best-fit model, model 25 from Hoeflich et al. (2017, 2023). The abundances are stratified, with asymmetries limited to the outer edge of the quasi-statistical equilibrium and nuclear statistical equilibrium layers in velocity. EC marks the region of electron capture elements, with the thin red line being ^{58}Ni. Right: angle-averaged energy deposition by γ-rays and positrons, E_X, for our reference model with (ρ_c, B) = (1.1×10^9 g cm^{-3}, 10^6 G; red). Also shown are explosion models with a large ρ_c (4×10^9 g cm^{-3} and $B = 10^6$ G; cyan) and a lower WD initial magnetic field (1.1×10^9 g cm^{-3}, 10^3 G; blue). Note that the shift of the sharp drop of E_X corresponds to the inner edge of the ^{56}Ni distribution as a function of ρ_c (Diamond et al. 2015). Positron transport effects become important for small B. E_X in the central electron capture region depends sensitively on the magnetic B-field. As a result, the emission from electron capture elements will change by a factor of 2. Though a large ρ_c increases the ^{58}Ni production by a factor of 2, the specific energy input is halved, leading to similar electron capture line strengths in the corresponding features. The degeneracy can be broken by line profiles with a resolution of better than 1000 km s^{-1} or a time series of data and models that cover the γ-ray to the positron-dominated regime. The excitation in the Ar region depends sensitively on the magnetic field of the WD, which has consequences for the spectra and a profound impact on the Ar line profiles (see Section 6.3).

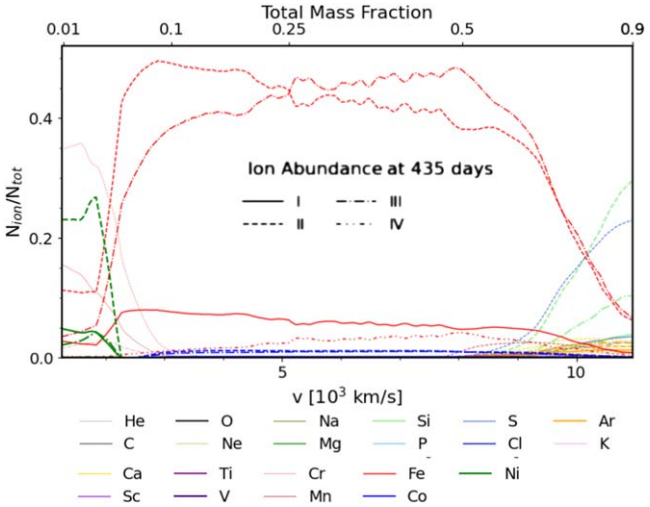

Figure 12. Same as the left panel from Figure 11 but with the angle-averaged ionization levels of I–IV per particle zoomed in on the spectrum-forming region. At day +415, most of the ^{56}Co (blue) has decayed to ^{56}Fe, with II and III being the dominant ionization stages where a small amount of I/IV is present. Various isotopes of electron capture elements (Fe/Co/Ni) are found in stages I–III and seen at low velocities.

Table 3
Model 25 Parameters

Parameter	Mod. 25a	Mod. 25b	Mod. 25	Mod. 25c	Mod. 25d
M_{ej} ($M_\odot$)	1.30	1.33	1.35[a]	1.35	1.38
ρ_c (10^9 g cm^{-3})	0.5	0.9	1.1[a]	1.1	4.0
M_{tr} ($M_\odot$)	0.24	0.24	0.24[a]	0.24	0.24
M_{DDT} ($M_\odot$)	0.5	0.5	0.5[a]	0.5	0.5
B (WD) (10^3 G)	1000	1000	1000[a]	1	1000

Note.
[a] Base model 25 is used as a reference.

Table 4
Line Contributions to the JWST Spectrum at Day +415 from the Reference Model with $\rho_c = 1.1 \times 10^9$ g cm^{-3} and $B = 10^6$ G

S	λ (μm)	Ion	S	λ (μm)	Ion	S	λ (μm)	Ion	S	λ (μm)	Ion	S	λ (μm)	Ion
	4.8603	[Fe III]	**	4.8891	[Fe II]		5.0623	[Co I]		5.1635	[Co I]		5.1796	[Co II]
**	5.1865	[Ni II]		5.2112	[Co I]	**	5.3402	[Fe II]		5.4394	[Co II]		5.4652[a]	[V I]
**	5.6739	[Fe II]	*	5.6870[a]	[V I]		5.7044	[Co II]		5.7391	[Fe II]	**	5.8933	[Ni I]
	5.9395	[Co II]	*	5.9527	[Ni II]	*	6.2135	[Co II]		6.273	[Co I]		6.2738	[Co II]
	6.3683	[Ar III]		6.379	[Fe II]	***	6.636	[Ni II]		6.7213	[Fe II]	**	6.9196	[Ni II]
**	6.9853	[Ar II]		7.0454	[Co I]		7.103	[Co III]	*	7.1473	[Fe III]		7.2019	[Co I]
*	7.3492	[Ni III]	**	7.5066	[Ni I]	*	7.7906	[Fe III]		8.044	[Co I]	*	8.211	[Fe III]
	8.2825	[Co I]	*	8.2993	[Fe II]	***	8.405	[Ni IV]	*	8.6107	[Fe III]	*	8.6438	[Co II]
*	8.7325	[Fe II]	*	8.9147[a]	[Ti II]	**	8.945	[Ni IV]	**	8.9914	[Ar III]	*	9.1969[a]	[Ti II]
	9.279[a]	[Co IV]	*	9.618	[Ni II]		9.8195	[Co I]	*	10.08	[Ni II]	**	10.1637[a]	[Ti II]
**	10.189	[Fe II]		10.203	[Fe III]	*	10.5105	[Ti II]	*	10.5105	[S IV]	*	10.523	[Co II]
**	10.682	[Ni II]	**	11.13	[Ni IV]		11.167	[Co II]	*	11.238[a]	[Ti II]		11.307	[Ni I]
***	11.888	[Co III]	**	12.001	[Ni I]	*	12.1592[a]	[Ti II]	**	12.255	[Co I]	*	12.261	[Mn II]
**	12.286[a]	[Fe II]	**	12.642	[Fe II]		12.681	[Co III]	**	12.729	[Ni II]		12.736	[Ni IV]
	12.811	[Ne II]		13.058	[Co I]		13.82	[Co III]		13.924[a]	[Co IV]		14.006	[Co III]
	14.356	[Co I]		14.391	[Co I]	*	14.739	[Co II]	*	14.814	[Ni I]	*	14.977	[Co II]
*	15.459	[Co II]		16.299	[Co II]	*	16.391	[Co III]	*	16.925	[Co I]	***	17.936	[Fe II]
*	18.241	[Ni II]		18.265	[Co I]	*	18.39	[Co II]	**	18.713	[S III]		18.804	[Co II]
	18.985	[Co II]	*	19.007	[Fe II]	**	19.056	[Fe II]		19.138	[Ni II]		19.232	[Fe III]
	20.167	[Fe III]		20.928[a]	[Fe II]		21.17[a]	[Fe I]		21.986[a]	[Fe II]		22.106[a]	[Ni I]
*	21.481	[Fe II]		20.167	[Fe III]		20.928[a]	[Fe II]		21.17[a]	[Fe I]		21.986[a]	[Fe II]
	22.106[a]	[Ni I]	*	21.481	[Fe II]	*	21.829	[Ar III]	*	22.297	[Fe I]		22.80[a]	[Co IV]
*	22.902	[Fe II]	***	22.925	[Fe III]		23.086	[Ni II]	*	23.196	[Co II]		23.389	[Fe III]
	24.04[a]	[Co IV]	***	24.042	[Fe I]	**	24.07	[Co III]	***	24.519	[Fe II]		24.847	[Co I]
**	25.249	[S I]	*	25.689	[Co II]	**	25.89	[O IV]		25.986	[Co II]	***	25.988	[Fe II]
	26.1	[Co III]		26.13	[Fe III]		26.601	[Fe II]		27.53	[Co II]		27.55	[Co I]
*	28.466	[Fe I]		29.675	[Mn II]	***	33.038	[Fe III]		33.481	[S III]		34.66	[Fe II]
*	34.713	[Fe I]	**	34.815	[Si II]	***	35.349	[Fe II]	*	35.777	[Fe II]	*	38.801	[Fe I]
	39.272	[Co II]	***	51.301	[Fe II]	***	51.77	[Fe III]	*	54.311	[Fe I]	*	56.311	[S I]
	60.128	[Fe II]												

Note. The relative strengths are indicated by the number of asterisks.
[a] Transitions without known lifetimes for which $A_{i,j}$ are assumed from the equivalent iron levels.

of the reasons for the lower ionization is that temperatures decrease by ∼1000–1500 K at day +415 from ∼5000 K at day 200–300 (Kozma & Fransson 1992; Fransson & Jerkstrand 2015). The temperature structure of SN 2021aefx at +415 days resembles an underluminous SN Ia at about 190 days (Hoeflich et al. 2021).

The significant difference between the new spectrum of SN 2021aefx and the previous ones is that +415 days marks the transition from the energy input being dominated by hard γ-rays to being dominated by positrons. This will be fully reached at ∼+500 days (Penney & Hoeflich 2014). Note that this time also corresponds to a shift in optical emission properties in SN 2011fe (Tucker et al. 2022). Hence, the magnetic field of the WD is a critical variable in the nebular simulations (Penney & Hoeflich 2014). We also note that in our models, between 400 and 500 days, γ-rays are just as important as positrons to the energy position in the most central regions, and both have a significant effect on the spectral formation.

6.3. Flux Spectra and Profiles

6.3.1. Atomic Data, Line Identifications, and Strengths

The atomic data used in our simulations come from Diamond et al. (2015, 2018), van Hoof (2018), and references therein. In addition, the atomic data have been supplemented by fits of the lifetimes, A_{ij}, of unknown weak features between 5 and 27 μm based on the observed spectrum (see Appendix C, Tables E1 and E2). Full lists with line strengths of transitions contributing to the flux spectrum of SN 2021aefx at +415 days from maximum are shown in Tables 4 and D1. Line IDs are only shown for transitions with measured spontaneous lifetimes, i.e., Einstein A_{ij} values. Our atomic models have been verified and used in previous papers (DerKacy et al. 2023a, 2024a) and cross-checked with line identifications by Kwok et al. (2023).

6.3.2. Understanding the Overall Spectra and Evolution

The observed and modeled spectra are presented with identifications of notable features in Figure 13. Here, we discuss the overall spectrum and underlying physics of our reference model before optimizing the parameters. The synthetic spectrum agrees reasonably well with the observations.

At first glance, the spectrum at +415 days resembles earlier epochs. However, this apparent similarity masks a physical regime change in the ejecta. For example, at +415 days, most of the radioactive ^{56}Co has decayed to ^{56}Fe (Figure 11), with only ∼2% of the initial ^{56}Co remaining. The observed and model spectra show broad features of [Fe II] and [Fe III] at 18 and 23 μm. In the models, the +415 day spectrum shows an equally strong, peaked feature at the location of [Co III] 11.888 μm rather than the rounded profile seen a year earlier. This is also seen in several weaker features, which could be attributed to [Co II] (e.g., 10.5 μm) at earlier epochs. Furthermore, the observed spectrum and model at +415 days

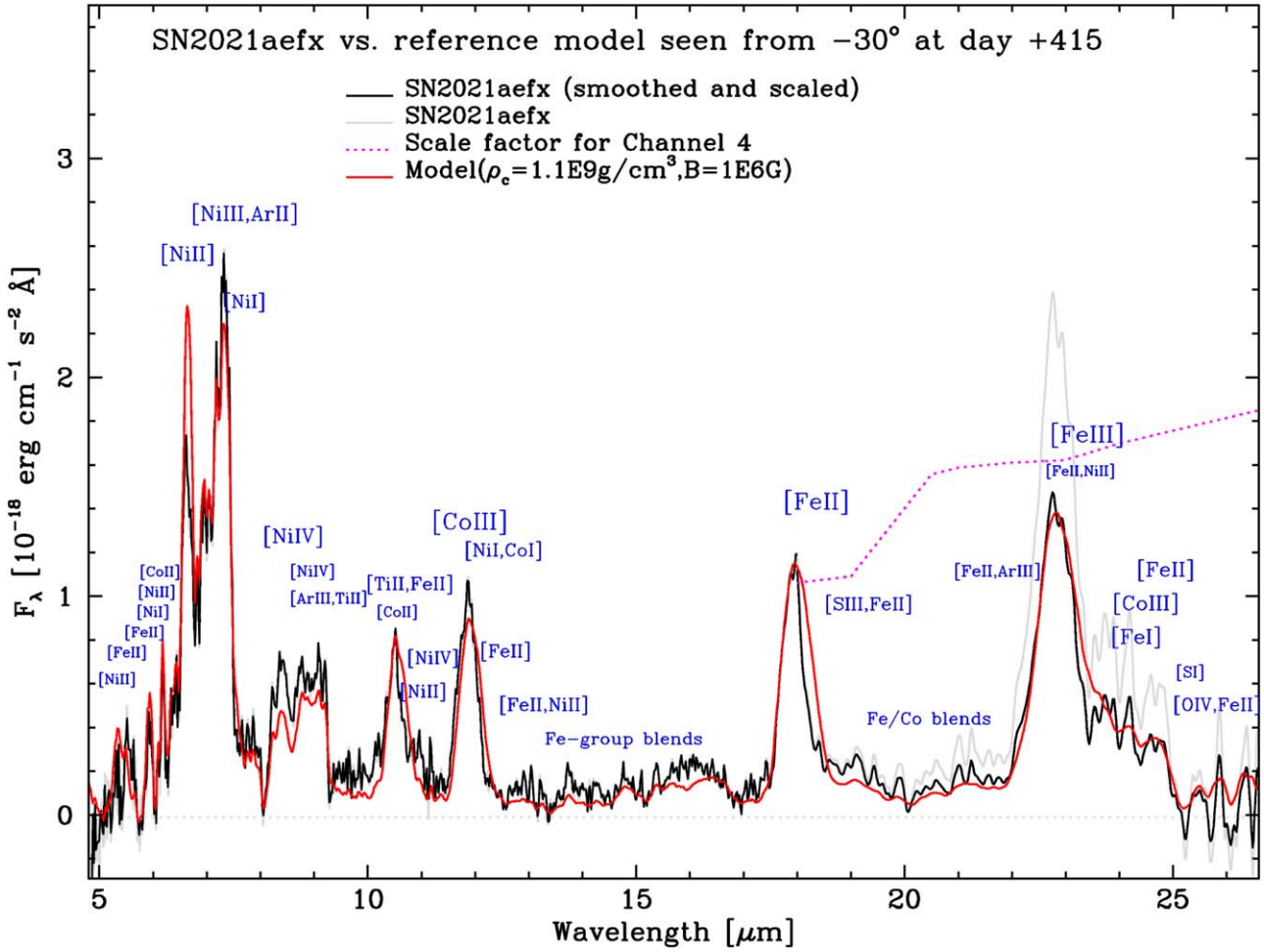

Figure 13. Comparison of the overall synthetic MIR spectra of our off-center reference model 25 seen from −30° and the JWST MIRI/MRS smoothed (black) and raw (gray) spectra of SN 2021aefx at +415 days relative to *B*-band maximum. The synthetic flux has been calibrated to the observed flux by adjusting the distance and using *M*–*m* to 31.64 mag. In addition, the scaling factor (magenta) is shown as applied to channel 4. This is appropriate because the background reduction in channel 4 is highly uncertain. The size of the labels for the contributions corresponds roughly to the line strength. Most of the MIR features show a complex structure and peaked morphology. This comes from a combination of blending and a contribution of electron capture elements. The observations agree reasonably well with the synthetic spectrum, though some shortcomings are apparent (see Section 6.4).

also show strong features at 7 and 9 μm. This is similar to earlier epochs, but both the profile shapes and dominant lines in the features have changed. At earlier times, the dominant ions have been identified as [Ar II] and [Ar III] (Gerardy et al. 2007; Telesco et al. 2015; DerKacy et al. 2023a; Kwok et al. 2023). In fact, at +415 days, the 8.991 μm feature is "flat-topped" rather than "flat-tilted," as was seen at earlier epochs. As we discuss below, the change in the profiles is not only caused by a spectral resolution effect (LRS versus MRS) but hints toward a physical regime change at this epoch.

Our reference model can reproduce the 10.5 μm feature reasonably well and is dominated by forbidden, singly ionized Fe, Ti, and Ni lines. Strong features at 7 and 9 μm are still there but are now dominated by Ni I–III and Ni IV, respectively, with Ar being only a minor contributor. There is a second distinct spectral component consisting of many narrow features such as Fe, Co, and Ni between 5 and 7 μm. These lines are well-known indicators of high-density burning ($\rho \geqslant 10^8$ g cm^{-3}; e.g., Seitenzahl & Townsley 2017) and, being narrow, show that there is little or no mixing in the ejecta close to the center.

The combination of line blending and the presence of two distinct spectral components, wide and narrow, is key to understanding the profiles and their evolution. Narrow lines of stable Ni are seen to dominate throughout because they produce sharply peaked line profiles. Sharp profiles can also be produced by overlapping broad lines if the separation is small compared to the peak width, as demonstrated for the Fe/Co complex at 1.26 μm (Diamond et al. 2018; Hoeflich et al. 2021). However, here, the small peaks are common in many lines with different blends.

6.3.3. The [Co III] 11.888 μm Evolution

As shown in Section 5.1, to first order, the peak emission of the [Co III] 11.888 μm feature follows the radioactive decay of ^{56}Co, as can be expected if the energy is deposited locally (e.g., by positrons) regardless of the distribution of elements (see Figure 7). Because this line transitions to the ground state, the total emission is a direct measure of the ionization by hard radiation and nonthermal leptons independent of the temperature and other model details (Telesco et al. 2015), very similar to the [Fe II] 1.644 μm feature (Höflich et al. 2004; Diamond et al. 2015; Kumar et al. 2023). In principle, the total ^{56}Ni mass can be determined by the total line flux. This approach has been tried based on optical spectra but with mixed results due to the temperature dependence of the optical transitions (Childress

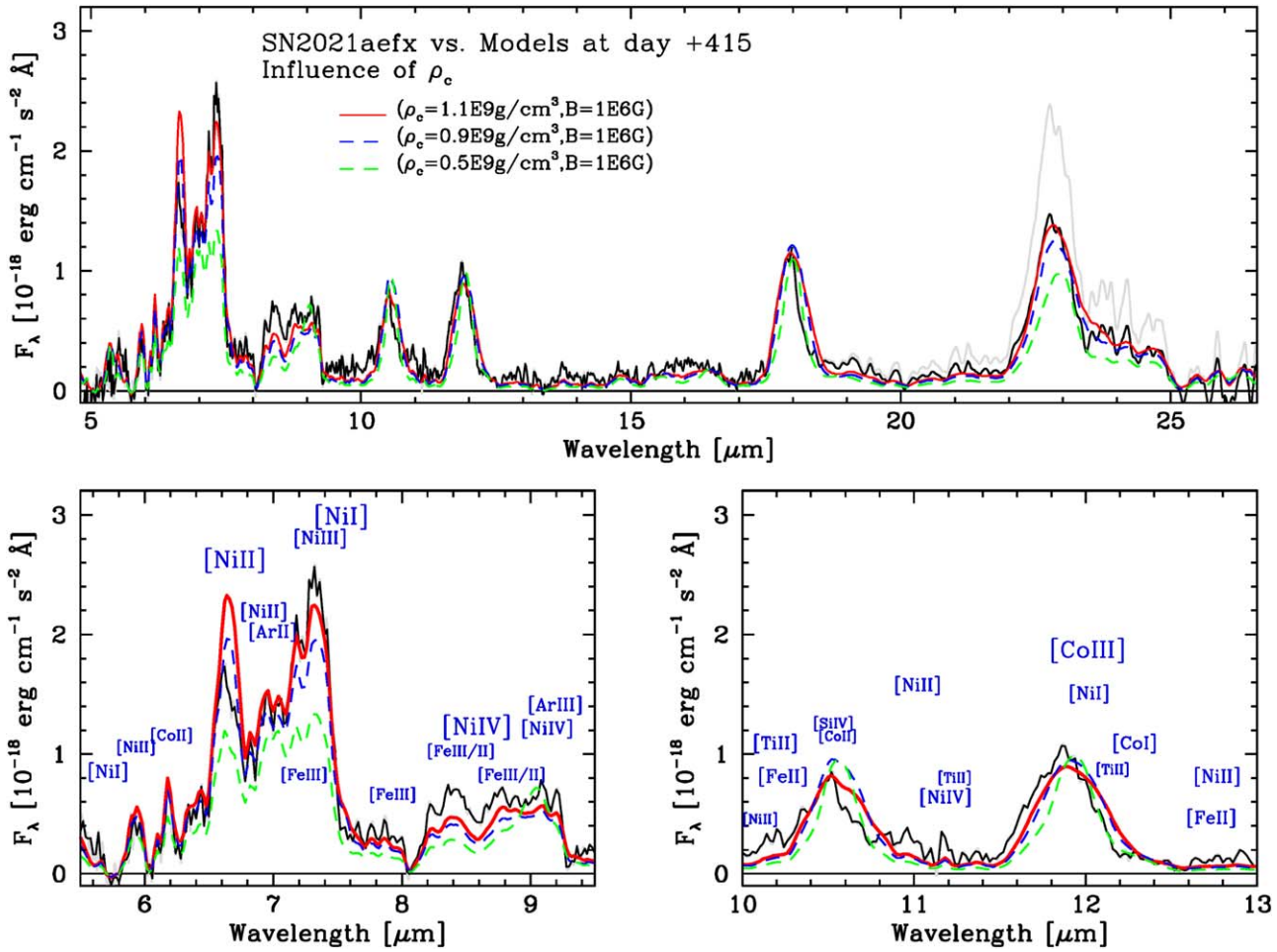

Figure 14. Same as Figure 13, but the sensitivity of the WD central density ρ_c on the synthetic spectra is shown. The lower plots show the zoomed regions of 5.5–9.5 μm (left) and 10–13 μm (right), respectively. Note the sensitivity of ρ_c on the overall 7 and 9 μm features, which is mostly a result of the decreasing ^{58}Ni abundance and the change in the line ratio at, e.g., 11.8 vs. 10.5 μm.

et al. 2015). This problem is not present when using the [Fe II] 1.644 μm and [Co III] 11.888 μm features.

Analysis of the absolute flux in this [Co III] is an important test for the treatment of nonthermal leptons and the production of ^{56}Ni. The overall quality of the spectral fits and fluxes may hint that our treatment is reasonably good. One limitation of the direct, model-independent application to determine or test the predicted ^{56}Ni mass is that the number of ionizations per bound–free absorptions by inner shell electrons will depend on the details of the atomic physics (Berger et al. 1998). Relative ^{56}Ni masses between SNe Ia should be reliable; however, the scaling factor between ionization and ^{56}Ni mass needs further validation, as discussed by Hoeflich et al. (2021).

The presence of small deviations in the peak fluxes of [Co III] relative to the true ^{56}Co decay (see Figure 7) hints at a more complex underlying physics. The relative contribution of γ-rays to positrons decreases with time, resulting in the center becoming optically thin and a change of the central peak of the feature. At day +415, γ-rays still contribute significantly to the energy input in the low-velocity center with electron capture elements (Figure 11), namely, ^{57}Co, ^{58}Ni, and ^{54}Fe. The isotopic shift between ^{56}Co and ^{57}Co is small, and the rest wavelengths of [Ni I] and [Co I] are similar to [Co III]. This leads to narrower additional components boosting the central peak of the 11.888 μm feature.

6.4. Sensitivity of the Free Parameters on the Spectra and Profiles

In this section, the formation of spectra and specific spectral profiles is considered in more detail and discussed in the context of variations between models.

6.4.1. Dependence on the WD Central Density

Figure 14 shows how the central density, ρ_c, of the WD (which determines the size of the inner ^{56}Ni hole and the amount of electron capture elements produced in the explosion) affects the spectral formation. With lower ρ_c, the intrinsic line profiles of ^{56}Fe and ^{56}Co become narrower because an increase of emission at low velocities produces a rise in the peak (Penney & Hoeflich 2014). This can be seen in the broad [Fe II]- and [Fe III]-dominated features at ≈18 and 23 μm. Note that, though a large ρ_c increases the ^{58}Ni production by a factor of 2, the specific energy input is halved, leading to similar electron capture line strengths but different widths in the features (Figure 11), resulting in similar strengths in the ^{58}Ni lines (Figure 14 versus 15). Furthermore, a high $\rho_c = 4 \times 10^9$ g cm^{-3} can be ruled out because it would produce profiles that are much broader than the data, by a factor of 2 based on a spherical model series (Diamond et al. 2015; Galbany et al. 2019). The MIR spectra of such densities are not shown here because our simulation does not have enough grid

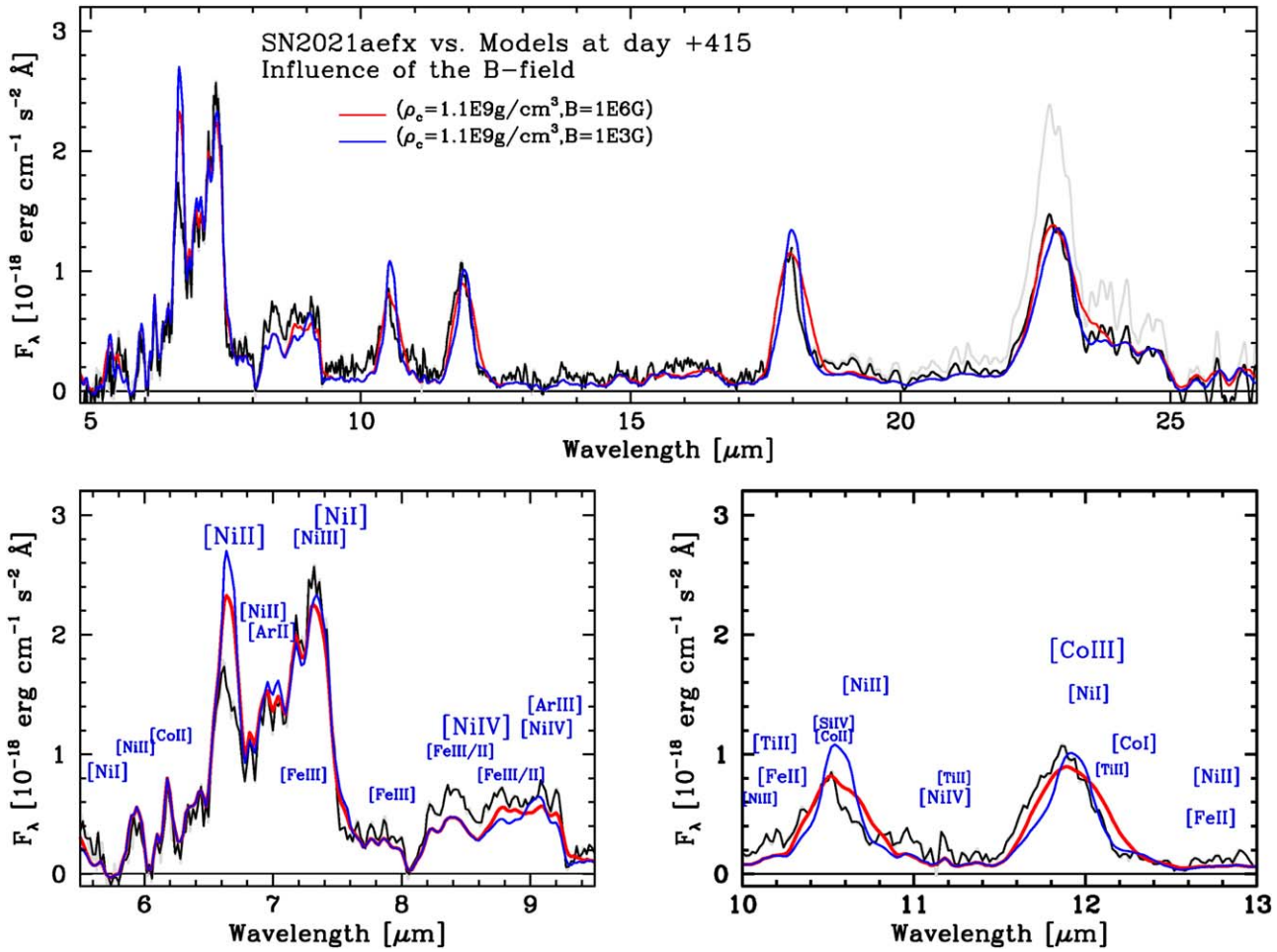

Figure 15. Same as Figure 14, but the sensitivity of the initial magnetic field of the WD, B, on the synthetic spectra is shown. The lines become narrower and more peaked with decreasing B. This is very similar to the low-ρ_c case. However, the effects can be separated by the overall spectral model.

points to resolve the complex radial structure of low Y_e electron capture elements such as Mn and Cr that are important (see Figures 25 and 26 in Galbany et al. 2019).

Another spectral indicator of the central density, ρ_c, is the trend that the features dominated by electron capture elements show a decreasing flux with decreasing ρ_c. This becomes obvious in the 6.7 and 7.4 μm regions. The sensitivity to ρ_c is also seen by narrow, mostly unblended weak [Ni II] and [Co II] lines at 6 and 6.2 μm, respectively.

Models with $\rho_c = 1.1$ and 0.9×10^9 g cm^{-3} do equally well at reproducing the observations. The former shows better agreement with the flux level, whereas the latter produces slightly narrower forbidden [Fe II] and [Fe III] features at 18 and 23 μm. Note that for $\rho_c \geqslant 0.9 \times 10^9$ g cm^{-3}, the total emission of Ni features hardly depends on the ^{58}Ni mass produced (in unmixed models) because the smaller electron capture core also increases the specific heating, which boosts the Ni emission (Figure 11). Because heating is produced by γ-rays and positrons, the degeneracy can only be broken by time series of spectra well beyond +500 days when positrons dominate everywhere. Moreover, at very late times, the variations due to positron transport effects can separate macroscopic from microscopic mixing.

Both the [Fe II] and [Fe III] features at 18 and 23 μm may favor the lowest ρ_c (0.5×10^9 g cm^{-3}). However, this model is incompatible with the features and profiles at 7, 10.5, and 12 μm due to the low mass of electron capture elements.

The 7 μm feature is complex, with a structure dominated by narrow Ni components with a width of $\sim$3000 km s^{-1} and a broad [Ar II] component (with a width of $\sim$7000–10,000 km s^{-1}) that "fills the emission gap" between the [Ni I]- and [Ni II]-dominated peaks. Other lines such as [Fe III] contribute to the complexity.

The emission complex between 8.1 and 9.3 μm shows two components. The blue part of this wavelength region ($\sim$8.4 μm) is dominated by [Ni IV] 8.405 μm. Observations and models of SN 2021aefx at +323 days show that the red part of this region ($\sim$9 μm) was dominated by [Ar III] (DerKacy et al. 2023a), which is similar to MIR observations of other SNe Ia (Gerardy et al. 2007; Telesco et al. 2015). At these phases, SN 2021aefx showed a tilted profile, which was interpreted as evidence for off-center DDT (DerKacy et al. 2023a). Such a profile can be tilted if the high-velocity region is asymmetric in the abundance distribution at the outer edge, e.g., produced by an off-center DDT (Hoeflich et al. 2021). However, in the latest spectrum of SN 2021aefx at +415 days, the 9 μm profile is "flat-topped," not tilted, and is dominated by [Ni IV] 8.945 μm and [Fe II]/[Fe III] lines with only a nondominant contribution of [Ar III]. This leads to a bump at the red end of the profile. Only about 50% of the red end of the profile comes from Ar and is produced after the transition to the

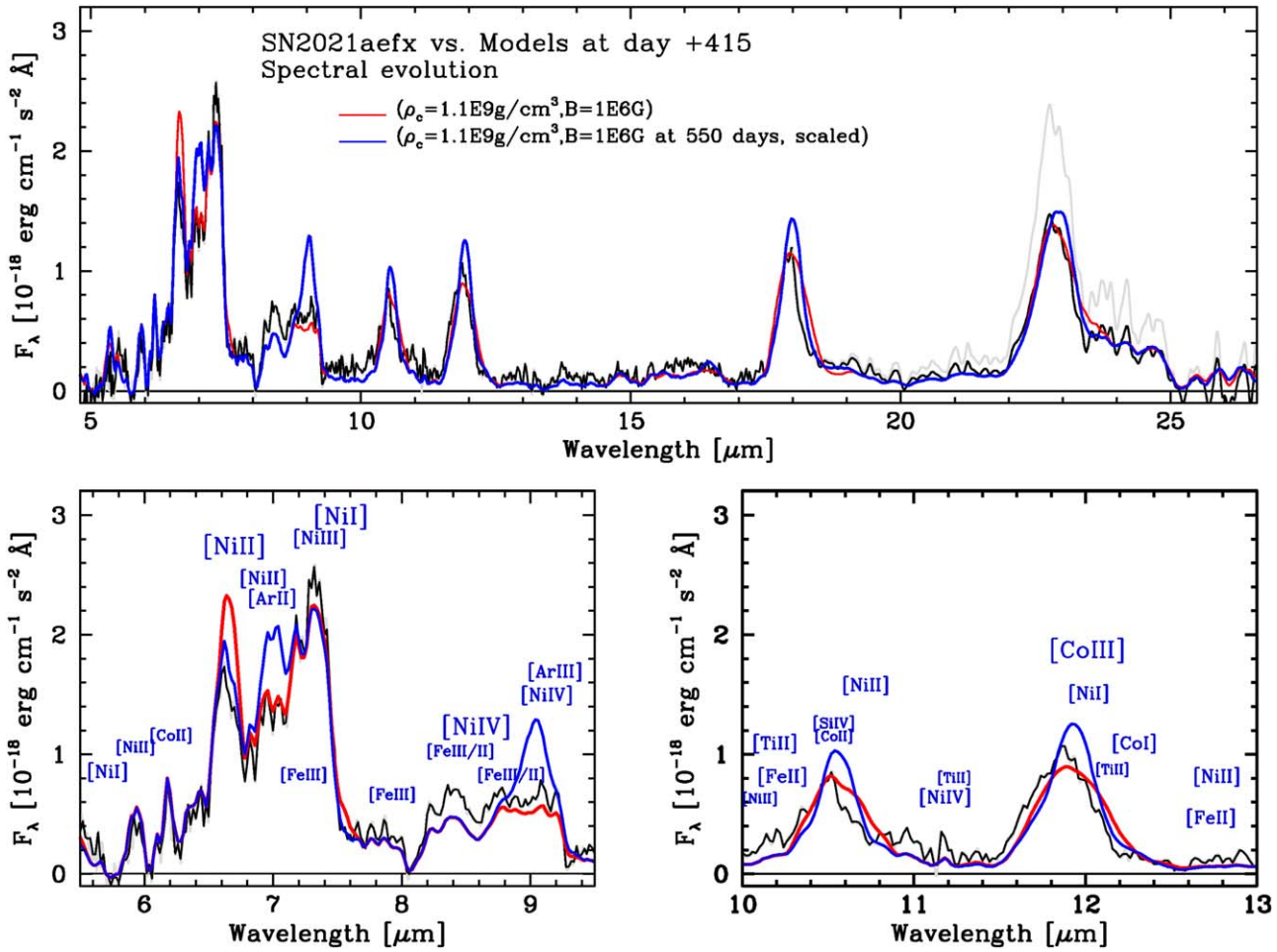

Figure 16. Same as Figure 14, but the evolution over one *e*-folding time for ^{56}Co decay is shown. The flux at +550 days is scaled up in luminosity to compensate for the ^{56}Co decay. Thus, line profiles and ratios between the models can be compared.

positron-dominated regime. The tilting vanishes because the outer, high-velocity Ar bulge is located outside the layers heated by positrons, resulting in a flat contribution to the profile at the latest epoch of observations.[38] About 50% of the total emission can be attributed to [Ni IV] and multiple lines of [Fe II] and [Fe III].

In the early nebular phase, blending by [Fe II] and [Fe III] was suggested as a main contributor to the [Ar III] feature. However, this leads to an opposite tilt to the observed spectrum (Blondin et al. 2023).[39] Thus, the tilt and evolution of the feature support our interpretation as a geometrical effect.

It is well established that the 12 μm feature at earlier times can be attributed to [Co III], although some weaker additional components are present. In the models by +415 days, [Ni I], [Ti II], and many weak Fe lines contribute about one-third of the flux. The significant contribution beyond [Co III] also becomes evident from Figure 14 by showing a pointed peak compared to earlier observations.

Overall, at +415 days, the ionization shifts toward lower ionization states with decreasing ρ_c. This is because for lower values of ρ_c, the ^{56}Ni region extends toward the more central layers (Diamond et al. 2015). This can be seen in the effect of the ratio of [Ni III] 7.35 μm/[Ni II] 6.92 μm features for various values of ρ_c. For 1.1×10^9 g cm^{-3}, this ratio is 1.7; for 0.9×10^9 g cm^{-3}, it is 1.5; and for 0.5×10^9 g cm^{-3}, the ratio is 1.1. Therefore, higher values of ρ_c are consistent with the observations.

However, the 7.35 μm versus 6.64 μm peaks are close to 1 for our simulations, whereas the observed value is about 1.3, which may reflect the limitation in either atomic physics or the underlying explosion models. Note that mixing of electron capture and ^{56}Ni layers will produce the opposite trend (DerKacy et al. 2023a) because with increasing ρ_c, the electron-capture-rich region increases in mass coordinates and into regions of Rayleigh–Taylor instabilities (see Section 6.6). Moreover, all the features in the 6–8 μm region are heavily blended. To derive ρ_c, the ratio between the peak of the [Co III] feature at 11.888 μm and the peak of the feature at 7.35 μm may be more appropriate. The corresponding value is 2.4 in both the observations and the model with $\rho_c \approx 1.1 \times 10^9$ g cm^{-3}, whereas the ratio is 1.2 for the low-density model.

As mentioned above, in both the models and data, most spectral features show a very narrow peak because they are dominated by electron capture elements but still have a broad component. This characteristic is valid for all strong Fe features

[38] At +323 days, heating was facilitated by γ-rays leading to a "flat-tilted" Ar-dominated profile.

[39] At +323 days, our simulations show blends at the same wavelength but weaker. If those blends dominate the profile, they would cause a tilt opposite to the observation.

in our model spectrum because the ^{56}Fe distribution traces ^{56}Co and ^{56}Ni.

We note that microscopic mixing (i.e., mixing of species on atomic scales) over large scales would drastically change the evolution and was previously excluded for SN 2021aefx (DerKacy et al. 2023a).

6.4.2. Dependence on the Initial Magnetic Field of the WD

Figure 15 shows the sensitivity of the initial magnetic field of the WD on the synthetic spectra. We use a turbulent morphology on scales of the Rayleigh–Taylor instabilities because even large-scale initial dipole fields would be tangled by passive flows during the deflagration phase of burning (Hristov et al. 2021). The changes of the spectra and profiles can be understood in the same way as the previous discussion. Prior to day ≈300, all positrons locally annihilate, regardless of the strength of the initial magnetic field of the WD (Penney & Hoeflich 2014). The changes in the specific energy distributions can be seen in Figure 11.

For weaker magnetic fields, positrons increasingly escape from the ^{56}Ni layers to regions of higher velocities. This leads to narrower mean half-width Fe and Co profiles, similar to changes in ρ_c, by reducing the emission at high Doppler shifts, namely, ^{56}Co at high velocities (see Figure 11). The second effect is a boost of features where quasi-statistical equilibrium elements, such as Si and S, contribute significantly to the line flux; e.g., see the feature at [Si IV] 10.5 μm, which is very similar to the potential appearance of the [Si II] 1.3 μm feature in the NIR (Diamond et al. 2015). The other effect is the shifting of the energy deposition toward the inner, higher-density layers, which results in a boost of the [Fe II] line at 18 μm compared to the [Fe III] at 23 μm, because some positron escape leads to slightly lower temperatures and thus a shift in the flux from the optical to the MIR (Penney & Hoeflich 2014; Mera Evans et al. 2022).

Though still high, a B-field of 10^3 G leads to strong leaking of positrons on both the inner edge and outer edge of the ^{56}Ni layers, which leads to a boost of [Ni II], strong pumping of [Si IV], and a shift in the ionization balance toward [Co II] (e.g., at 10.3 μm) compared to [Co III]. Similarly, the profile of the 9 μm features changes from flat-topped with a B-field of 10^6 G to a peaked profile with a B-field of 10^3 G. We require initial B-fields ≈10^6 G to keep the positron transport local, which is comparable with previous lower limits of 10^5 G derived from other SNe Ia (Höflich et al. 2004; Diamond et al. 2015; Hristov et al. 2021; Kumar et al. 2023). For the creation of high B-fields, we possibly need a strong dynamo during the smoldering phase, as discussed in the above publications.

6.4.3. Future Time Evolution of the Spectra

In the discussion in Section 5, we made use of past observations. From the models, we identified that the main physical driver of the evolution is the abundance change from ^{56}Co to ^{56}Fe and the change of the mode of energy input from a γ-ray- to a positron-dominated regime.

Here, we consider the future evolution of SN 2021aefx using the same model configuration and parameters presented above. This model has been evolved to one *e*-folding time of ^{56}Co later (+550 days; see Figure 16); hence, the absolute flux is lower. The main change in the evolution of the spectral profiles is a boost in features dominated by intermediate-mass elements, such as [Ar II] at 7 μm and [Ar III] at 9 μm. Furthermore, there is a narrowing of features due to a combination of positron transport effects and a decrease in the contribution from γ-rays by ≈60% produced by the geometrical dilution.

At +550 days, the spectrum resembles an SN Ia; however, not unexpectedly, it does not match the data from +415 days.

What would one learn if the prediction looked different from future data or the spectral evolution was slow? One would have to restore positron trapping by increasing the magnetic field of the WD because B decreases with the square of time. In general, positron transport effects on the spectra depend on the size and morphology of both the magnetic field and the 3D abundance distributions in the central region.

6.4.4. Observable Signatures of Off-center DDTs Prior to the Nebular Phase

Prior to the nebular phase, the off-center DDT has two major effects. (i) It influences the rise, strength, and profile of the [Co III] 11.888 μm feature during the transition from the photospheric to the nebular phase. This evolution has been identified as valuable diagnostics for the progenitor mass (Telesco et al. 2015). The rise is caused by the receding photosphere in combination with the rapidly dropping density (Penney & Hoeflich 2014) and, for asymmetric abundance distributions, will depend on the inclination. (ii) The DDT imposes a large-scale asymmetry in all abundances, including products of partial carbon and incomplete oxygen burning such as Mg/Si/S, which results in significant line polarization. This is frequently seen in the Si II 6355 Å feature in many normal-luminosity SNe Ia during the photospheric phase (Cikota et al. 2019). It can be understood by selective depolarization by lines in scattering-dominated atmospheres when seen from positive Θ (Yang et al. 2020; Hoeflich et al. 2023). Unfortunately, neither polarization measurements nor earlier MIR spectra were obtained for SN 2021aefx.

6.4.5. Progenitor Signatures in SN 2021aefx

The nebular spectrum presented provides a sensitive tool for studying the explosion mechanism and the thermonuclear runaway. As discussed in Section 5, the nebular spectra of SN 2021aefx closely resemble several normal SNe Ia. However, nebular spectra provide limited information about the donor star and progenitor systems unless a significant amount of material is stripped from the companion (Marietta et al. 2000). In our spectrum, all features have been identified without evidence for stripped material.

Early-time spectra and light curves of SN 2021aefx show high spectral velocities and an early blue bump, suggesting an additional energy source (Ashall et al. 2022; Hosseinzadeh et al. 2022; Ni et al. 2023). Observed early-time variation between SNe Ia suggests diversity in progenitor systems and in the pathways to the explosion. At early times, only 10^{-3}–10^{-4} $M_\odot$ of ejecta is visible (see Figure 11 of Hoeflich et al. 2023).[40] We refer to Section 6.1 of Hoeflich et al. (2023 and references therein) for a detailed discussion of possible imprints of the progenitor system and its environment on these early phases. In short, these imprints may come from (i) explosive surface burning of H/He of ∼10^{-3}–10^{-4} $M_\odot$

[40] Note that from early-time spectropolarimetry of SN 2019np, these corresponding layers have been found to be very asymmetric (Hoeflich et al. 2023).

triggered by the outgoing detonation wave for some progenitor channels within the delayed-detonation scenario (see Figure 3 of Hoeflich et al. 2019). This amount of He is very similar to progenitors with an accreting He star and is the minimum mass needed in He-triggered detonations in sub-M_{Ch} explosions (Fisher 2015; Roy et al. 2022). In both explosion scenarios, surface He burning would produce high-velocity burning to Si, S, Ca, and Ti. (ii) Interaction of the outgoing shock wave with the circumstellar matter, namely, a Roche lobe or a strong wind from a companion star, and (iii) stellar rotation of the WD. Note that, for SN 2021aefx, Figure 1 may suggest a dirty environment and, possibly, late-time interaction with the interstellar medium.

6.5. Discussion and Implications for the Underlying Explosion Physics

To prevent duplication of discussions on alternative scenarios, we direct readers to the analyses provided in earlier studies (Hristov et al. 2021; Hoeflich et al. 2023) and, for SN 2021aefx, to DerKacy et al. (2023a). Here, we focus on our new findings and their implications.

SN 2021aefx can be understood in the framework of an off-center delayed-detonation model with central WD densities of $\rho_c \approx 0.9$–1.1×10^9 g cm^{-3} and with $M_{WD} \approx 1.33$–$1.35\,M_\odot$. These parameters can be attributed to a near-M_{Ch}-mass WD and place it into a regime of high-density burning with a proton-to-nucleon ratio $Y_e \approx 0.49$. As discussed at the beginning of Section 6 in the context of the model construction, the relatively low ρ_c requires a large accretion rate that may be more compatible with He or C rather than H accretors.

For the +415 day spectra, the strength of the ^{58}Ni hardly depends on the total mass of ^{58}Ni, which is governed by ρ_c. As is obvious from Figure 11, the amount of ^{58}Ni may vary by a factor of 2, but this can be compensated by the specific energy input, i.e., the energy input per gram. Time series of data and models are needed that cover the γ-ray-dominated nebular regime ($\sim$200 days) to the positron-dominated regime, which starts at $\sim$500 days after the explosion.

The result is that the main isotopes in the core are stable electron capture elements, e.g., ^{58}Ni, ^{57}Co, and ^{54}Fe. This places SN 2021aefx into a similar physical regime as other normal-luminosity SNe Ia such as SN 2014J (Telesco et al. 2015).

However, in our models, not all SNe Ia have the same ρ_c. In fact, they seem to span a wide range between 5 and 50×10^8 g cm^{-3}, where there is evidence for high ρ_c in subluminous SNe Ia such as SN 2016hnk, SN 2020qxp, and SN 2022xkq (Höflich et al. 2004; Penney & Hoeflich 2014; Diamond et al. 2015, 2018; Galbany et al. 2019; DerKacy et al. 2024a).[41]

Probing the transition between the γ-ray- and positron-dominated regimes is important for establishing the Urca process, its inner workings, its impact on the energy balance during the smoldering phase, and the nature of weak interactions (see Diamond et al. 2018; Tucker et al. 2022, and references therein). Moreover, nuclear cross sections played a role (e.g., Brachwitz et al. 2000; Höflich et al. 2006) and will continue to play a central role (Thielemann 2019) in our understanding of the explosion mechanism and thermonuclear runaway. For example, improvements in the electron capture rates (Langanke & Martínez-Pinedo 2000) resulted in a drastic change of the [Fe II] at 1.644 μm nebular line profile (Höflich 2006) from flat-topped to rounded (Penney & Hoeflich 2014), which demonstrated the need for high-ρ_c WDs close to where an accretion-induced collapse would occur (e.g., Gronow et al. 2021).

6.6. Implications for the Physics of the Thermonuclear Runaway

The comparison of synthetic and observed spectral profiles places strong constraints on the thermonuclear runaway in the delayed-detonation scenario, specifically regarding the initiation of thermonuclear explosive burning.

Detailed multidimensional simulations of the central single-point runaway show only mixing of the inner electron capture layers during the deflagration phase (see, e.g., Figures 1, 2, and 15 in Khokhlov 2000). Mixing occurs only during the subsonic deflagration phase and not during the subsequent detonation phase of DDT models, which leads to overall structures very similar to spherical DDT models (see Figure 3 in Gamezo et al. 2005). In contrast, multiple-spot, off-center ignitions mix the electron-capture-rich material to high velocities (Fink et al. 2014; Pakmor et al. 2024). The differences between these hydrosimulations can be simply understood by the lack of gravitation in the center, which results in close-to-laminar burning for about 1 s of high-density burning before Rayleigh–Taylor instabilities develop, whereas in multispot far off-center ignitions, the Rayleigh–Taylor-dominated burning phase starts right away. As shown by Khokhlov (2000), the long delay between ignition happens regardless of preexisting turbulence produced during the smoldering phase (Höflich & Stein 2002) or low C/O ratios (e.g., Domínguez et al. 2001). Preexisting turbulence will introduce some mixing by dragging material, but this effect is limited to the innermost slowly expanding layers. As found in the analysis of previous SNe Ia (Galbany et al. 2019; Hoeflich et al. 2021), again the spectra here are consistent with a near-to-central ignition and inconsistent with multispot strong off-center ignition.

Moreover, the narrow width of the lines produced by electron capture elements puts tight limits on the macroscopic mixing and confines it to the inner $\approx$3000 km s^{-1}, which may be expected from the passive drag of electron capture material by preexisting turbulent fields produced during the smoldering phase (e.g., Höflich & Stein 2002). Note that high WD magnetic fields ($B \geqslant 10^6$ G) are required based on studies of light curves[42] and spectra. Such fields may decrease the mixing of electron capture elements even further. For detailed discussions, see Höflich et al. (2004), Diamond et al. (2015), Hristov et al. (2021), Hoeflich et al. (2023), and DerKacy et al. (2024a). A turbulence field can be expected to develop during the smoldering phase (Höflich & Stein 2002), which drags the freshly formed products of high-density burning by passive flow. The result is an inhomogeneous mixture of nonradioactive electron capture elements and ^{56}Ni material that is heated over days by radioactive decay. Pressure equilibrium will compress the electron capture elements and nonradioactive layers into thin sheets (Hoeflich 2017). Preexisting turbulence

[41] High central densities, close to an accretion-induced collapse, found in many SNe Ia do not imply one specific unique explosion/progenitor scenario for all SNe Ia.

[42] To measure B-fields of the order of 10^6 G, an accuracy of 0.025 mag is required for late-time bolometric light curves (Hristov et al. 2021).

may produce caustic distributions with a wall thickness of $\approx$1000–1500 km s^{-1} but limited to the inner region (Fesen et al. 2015; Hoeflich 2017). The models used here do not take these structures into account, but their existence has been recently indicated by late-time polarization (Yang et al. 2022).

7. Conclusions

We present nebular phase JWST MIRI/MRS observations of SN 2021aefx at +415 days past maximum. Our work demonstrates how combining MIR medium-resolution data with detailed spectral models allows for the physics of SNe Ia to be understood in a way that was previously not possible. JWST promises to transform this area of research over the coming years. The main results of our study can be summarized as follows.

1. These new data and models covering 5–27 μm have allowed us to produce an extended list of line identifications during the iron-dominated nebular phase (see Section 2 and Table 4). The higher resolution of the spectrum relative to previous epochs has allowed for many spectral features to be resolved. The spectrum is dominated by iron-group elements, with a strong contribution of stable Ni.
2. The JWST MIRI/MRS spectrum at +415 days has been analyzed in conjunction with previous MIRI/LRS observations of SN 2021aefx, allowing for a time series analysis from +255 to +415 days to be performed. We find that the peak evolution of the resonance [Co III] 11.888 μm feature is consistent with the half-life of radioactive decay of ^{56}Co (see Section 5.1 and Figure 7).
3. The spectrum has been analyzed using a new series of off-center delayed-detonation models. All models had a central point of ignition and a point of the DDT at 0.5 $M_{\odot}$, which results in asymmetric abundance distributions (see Section 6). The viewing angle Θ is measured between the line of sight and the line defined by the point of DDT and the kinematic center. The spectrum at +415 days can be reproduced using the same $\Theta \approx -30^{\circ}$ that has been found in our previous study of SN 2021aefx at +323 days (DerKacy et al. 2023a). For other SNe Ia, a wide range of values for Θ from -90° to $+90^{\circ}$ have been found between SNe. This supports our interpretation that the profiles of SN 2021aefx are produced by a geometric effect.
4. Variations in the central density and initial magnetic field of the WD in the models were studied. We find that the progenitor of SN 2021aefx had a WD mass of $\approx$1.33–1.35 $M_{\odot}$, a central density of $\rho_c = 0.9-1.1 \times 10^9$ g cm^{-3}, and an initial magnetic field of $\geqslant 10^6$ G.
5. Comparison between these new data and models has revealed a profound change in the physics of the spectral formation compared to previous epochs. At +415 days, the SN made the transition from a ^{56}Co-dominated to a mostly ^{56}Fe-dominated regime. For the energy input, this is the transition phase from a globally γ-ray-dominated regime toward a positron-dominated regime. However, at +415 days, γ-rays still dominate the energy input in the central region. The evolution of the line profiles can be understood in terms of the above physics (see Section 6.4).
6. The fact that we observe a narrow region of electron capture elements means there is very limited mixing in the inner regions of the ejecta. Thus, the point of ignition in SN 2021aefx is consistent with being near-to-central and inconsistent with being strongly off-center if burning started as a deflagration front (see Section 6.6).
7. At +415 days, the strength of the Ni features is dominated by the size of the B-field in the WD and is rather insensitive to the amount of Ni produced through high central density burning $\geqslant 10^9$ g cm^{-3}.
8. At earlier epochs, the spectral features at 7 and 9 μm were mostly attributed to [Ar II] and [Ar III]. The profiles were interpreted as being caused by asymmetric abundance distribution produced by the off-center nature of the DDT. This resulted in a "flat-tilted" line profile because the entire Ar region was excited by γ-rays. At +415 days, these features have significantly changed. The Ar region is no longer excited by γ-rays but by positrons, which deposit their energy locally. Hence, the emission is governed by the overlapping region between ^{56}Ni and Ar. The Ar contribution to the 7 and 9 μm features is small and flat-topped, because the contribution of the asymmetric component from the outer layers is suppressed relative to earlier epochs. Overall, these features are dominated by iron-group elements at this phase (Section 6.4).
9. Spectra and line profiles are sensitive to the initial B-field of the WD because positron transport alters the energy input relative to the abundances (Penney & Hoeflich 2014; Diamond et al. 2015). Here, the importance of positron transport and the need for high B-fields has been demonstrated, where we find the need for B-fields that are larger than the fields typically found in WDs. These values of B may be produced during the smoldering phase prior to the explosion. Later time spectra are needed to push the limits to the regime where they heavily modify the properties of nuclear-burning fronts (Remming & Khokhlov 2014; Hristov et al. 2018).

Finally, we want to emphasize the future prospects for our analysis of SN 2021aefx. After about 550 days, the spectra enter the full positron-dominated regime. The positron transport effects have been demonstrated and the lower limit of B has been derived for SN 2021aefx, but spectra taken after day 700 (DerKacy et al. 2023b, 2024b) will be more sensitive to the morphology of the magnetic field of the WD and will provide the measurements of B beyond the current limit of 10^6 G. Current JWST observations indicate a low-density and high-mass WD that had a high magnetic field. This hints toward both a lack of full understanding of the accretion and smoldering phase and the Urca cooling, which may be affected by large B-fields and WD rotation. Future JWST observations may address these problems.

Overall, SN 2021aefx has demonstrated how intensive studies with an extended time series of data consisting of low- and medium-resolution spectra can revolutionize our understanding of the physical processes governing SNe Ia. However, SN 2021aefx is just one object, and future low-to-medium-resolution JWST observations of SNe Ia are required to examine the true diversity within both the physical processes in the ejecta and the explosion scenarios within the Universe.

Acknowledgments

C.A., P.H., E.B., J.D., and K.M. acknowledge support by NASA grants JWST-GO-02114, JWST-GO-02122, JWST-GO-03726, JWST-GO-04436, and JWST-GO-04522. M.S. acknowledges support by NASA grants JWST-GO-03726, JWST-GO-04436, and JWST-GO-04522. Support for programs #2114, #2122, #3726, #4436, and #4522 were provided by NASA through a grant from the Space Telescope Science Institute, which is operated by the Association of Universities for Research in Astronomy, Inc., under NASA contract NAS 5-03127. P.H. and E.B. acknowledge support by NASA grant 80NSSC20K0538. P.H. acknowledges support by NSF grant AST-2306395.

L.G. acknowledges financial support from the Spanish Ministerio de Ciencia e Innovación (MCIN) and the Agencia Estatal de Investigación (AEI) 10.13039/501100011033 under the PID2020-115253GA-I00 HOSTFLOWS project, from Centro Superior de Investigaciones Científicas (CSIC) under the PIE project 20215AT016 and the program Unidad de Excelencia María de Maeztu CEX2020-001058-M, and from the Departament de Recerca i Universitats de la Generalitat de Catalunya through the 2021-SGR-01270 grant. I.D. is supported by the project PID2021-123110NB-I00 financed by MCIN/AEI /10.13039/501100011033/ & FEDER A way to make Europe, UE.

Facilities: JWST (MIRI/MRS), MAST (JWST).

Software: jwst (Bushouse et al. 2023), jdaviz (ver. 3.2.1, JDADF Developers et al. 2023), HYDRA (Höflich 2003b, 2009; Hoeflich et al. 2017), Astropy (Collaboration et al. 2013, 2018, 2022), NumPy (Harris et al. 2020), SciPy (Virtanen et al. 2020), Matplotlib (Hunter 2007).

Appendix A
Data Reduction

The data were reduced using a custom-built pipeline[42] designed to extract observations of faint point sources that have complex backgrounds in MIRI/MRS data cubes (see Shahbandeh et al. 2024). In short, the pipeline creates a master background based on 20 different positions away from the source within the field of view. This master background is subtracted from the whole data cube. The SN flux is then extracted along the data cube using the *Extract1dStep* in stage 3 of the JWST reduction pipeline. The resulting data cube subtraction is shown in Figure A1. All the previously unpublished data used in this paper can be found at MAST via doi:10.17909/f37y-gn67.

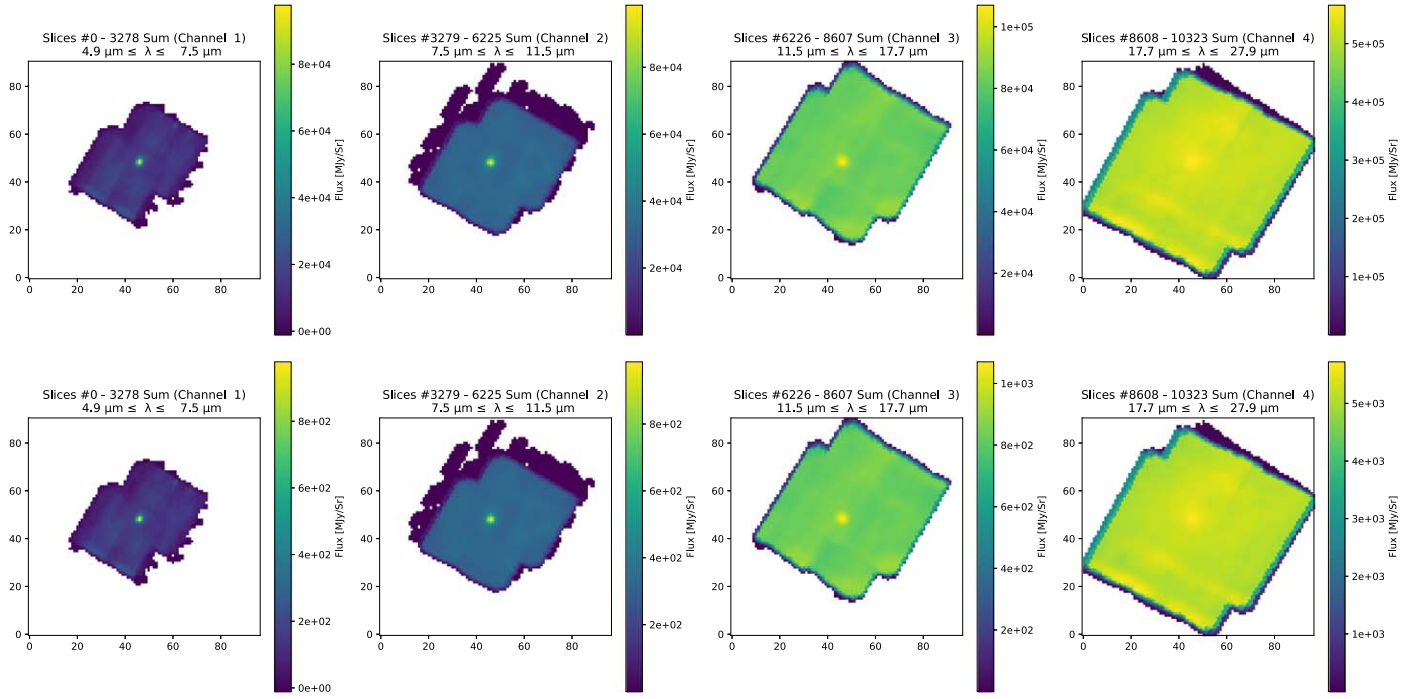

Figure A1. Top panels: MIRI/MRS cube of SN 2021aefx before background subtraction divided into four channels. Each channel is the collapsed sum of all its slices. Bottom panels: MIRI/MRS cube of SN 2021aefx after background subtraction.

[42] https://github.com/shahbandeh/MIRI_MRS

With this custom-made pipeline, the flux level in channel 4 (which covers wavelengths longer than 17.7 μm) is uncertain due to the dominant instrumental background flux, which increases with wavelength. Therefore, for the spectral analysis, we choose to extract the data from channel 4 separately using a manually selected background region to ensure that the continuum level is close to flat, as would be expected from a normal SN Ia in the nebular phase (see Appendix B for more details). We emphasize that this may cause large uncertainties in terms of line strengths and ratios in channel 4, and the reduction of channel 4 data may change as the JWST MIRI/MRS pipeline improves. The reduction shown here utilized version 1.9.4 of the JWST Calibration Pipeline (Bushouse et al. 2023) and Calibration Reference Data System files version 11.16.20.

Appendix B
Channel 4 Reduction

Due to the increased noise from the background in channel 4, we chose to manually extract the SN flux in this region. To do this, we use an STScI notebook[43] designed to perform extraction on a point source in JWST NIRSpec IFU data. We adapt this for use with MIRI/MRS data, using the final s3d data cube obtained from MAST. We extract the spectrum using a linearly expanding circular aperture (cone) because the PSF size increases with wavelength. The spectrum at the position of the SN is obtained by extracting the raw flux using apertures of various sizes at the location of the SN. After visual inspection, we chose to proceed with an aperture radius of 0.″273 (this is 1 pixel in radius). Although this aperture size is likely to be smaller than the true PSF of the SN, using a larger size dramatically increases the noise in the data. To remove the background contribution, individual background spectra are constructed at 32 locations away from the SN across the field of view. For each spectrum, the background is subtracted from the raw SN flux; see Figure B1. There is a large variation in the final flux depending on the location of the background selected. We opt to use a background where the continuum is roughly flat. Our chosen optimum background position is centered around pixels $x = 15$, $y = 23$.

Figure B2 shows the final SN spectrum in channel 4. Due to the small aperture, this spectrum has to be scaled by a factor of 6 to match the flux in channel 3. Overall, we highlight that the flux in channel 4 is uncertain, but we are confident in the width and location of the features identified. Finally, we note that combining all 32 background spectra before subtracting from the raw SN spectrum does not successfully remove the

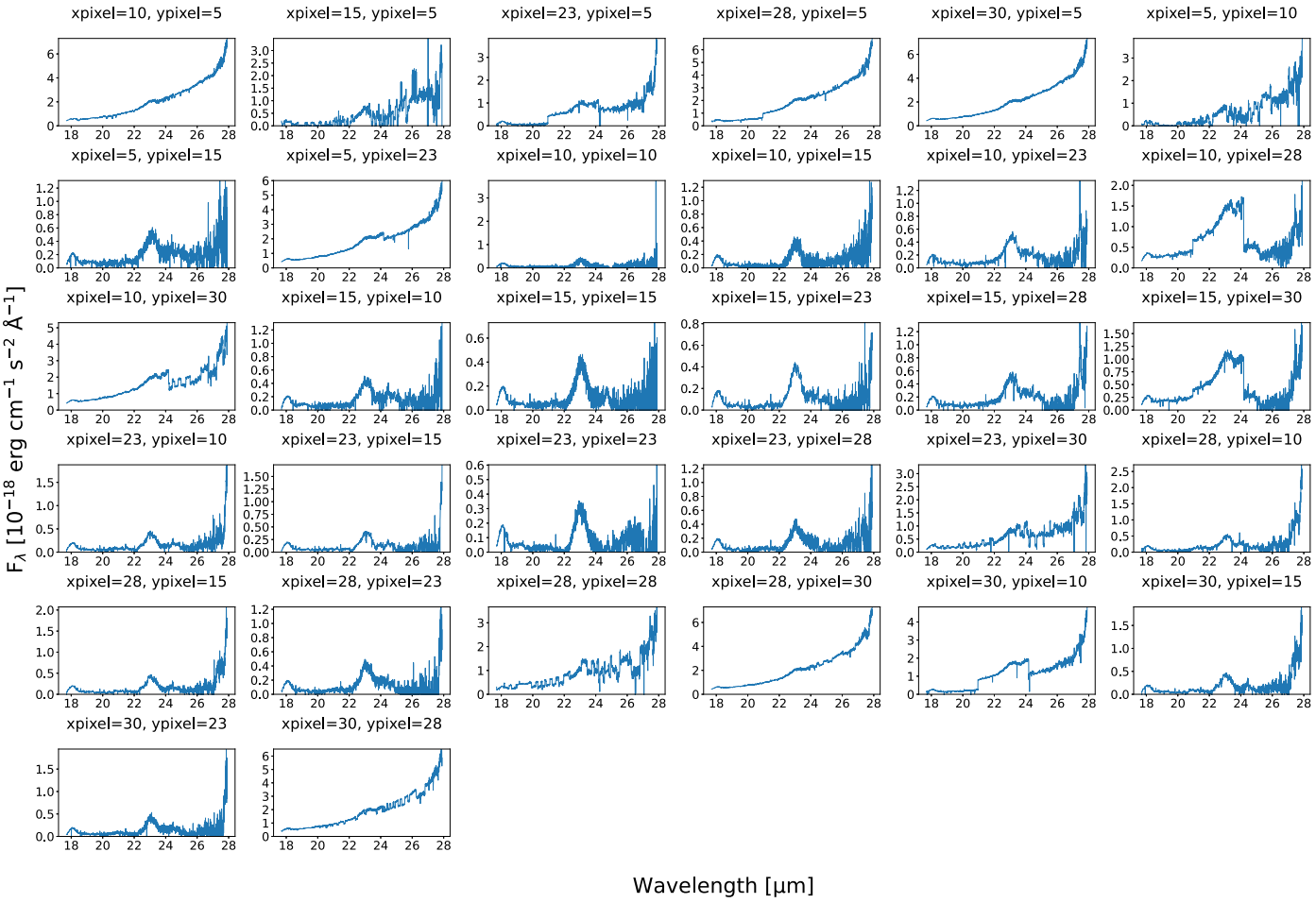

Figure B1. Thirty-two spectra extracted using different background positions within the IFU data cube.

[43] https://spacetelescope.github.io/jdat_notebooks/notebooks/ifu_optimal/ifu_optimal.html

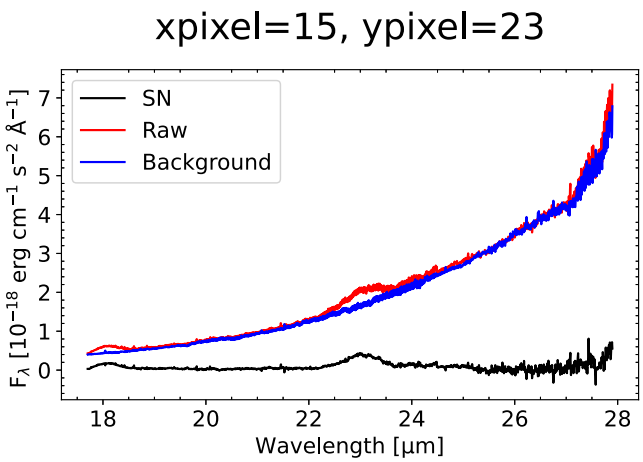

Figure B2. The raw flux at the position of the SN (red), with the flux at the position of the optimal background region centered on pixel $x = 15$, $y = 23$. The final channel 4, produced from subtracting the extractions, is plotted in black.

background flux and leaves a large excess at longer wavelengths.

Appendix C
Velocities

In this appendix, we fit spectral line profiles of the dominant ions in selected wavelength ranges to determine the region in the ejecta in which they are formed. As the spectral resolution of MIRI/MRS is much higher than the previous MIRI/LRS observations, this analysis has the potential to allow us to determine more accurately the location of the emitting regions within the ejecta. However, as discussed in the main text, many of the atomic line transitions are not known in this region, and detailed spectral modeling is required to make significant progress. Despite this, we fit the spectra below.

For the fitting process, the *scipy.optimize* package is used, and the best fits are determined via using the Levenberg–Marquardt algorithm and the least-squares statistic option. In each wavelength region, the emission features within the regions are assumed to be composed of Gaussian profiles. Although treating emission line profiles as Gaussians makes assumptions about the distribution of the material in the emitting region, it does provide us with a quantitative way to analyze the data. Priors and bounds are provided to each fit to ensure that they are consistent with the line IDs provided from the models in Section 6. If there is a region in which a line ID is not provided from the models, but there is a clear feature, we also add an emission profile in this region. The spectral fits can be found in Figure C1, and the corresponding values, plotted in Figure 10, are presented in Table C1. Finally, we choose not to fit the feature between 8 and 10 μm due to the complex blend around the "flat-topped" Ar region, and we do not fit longward

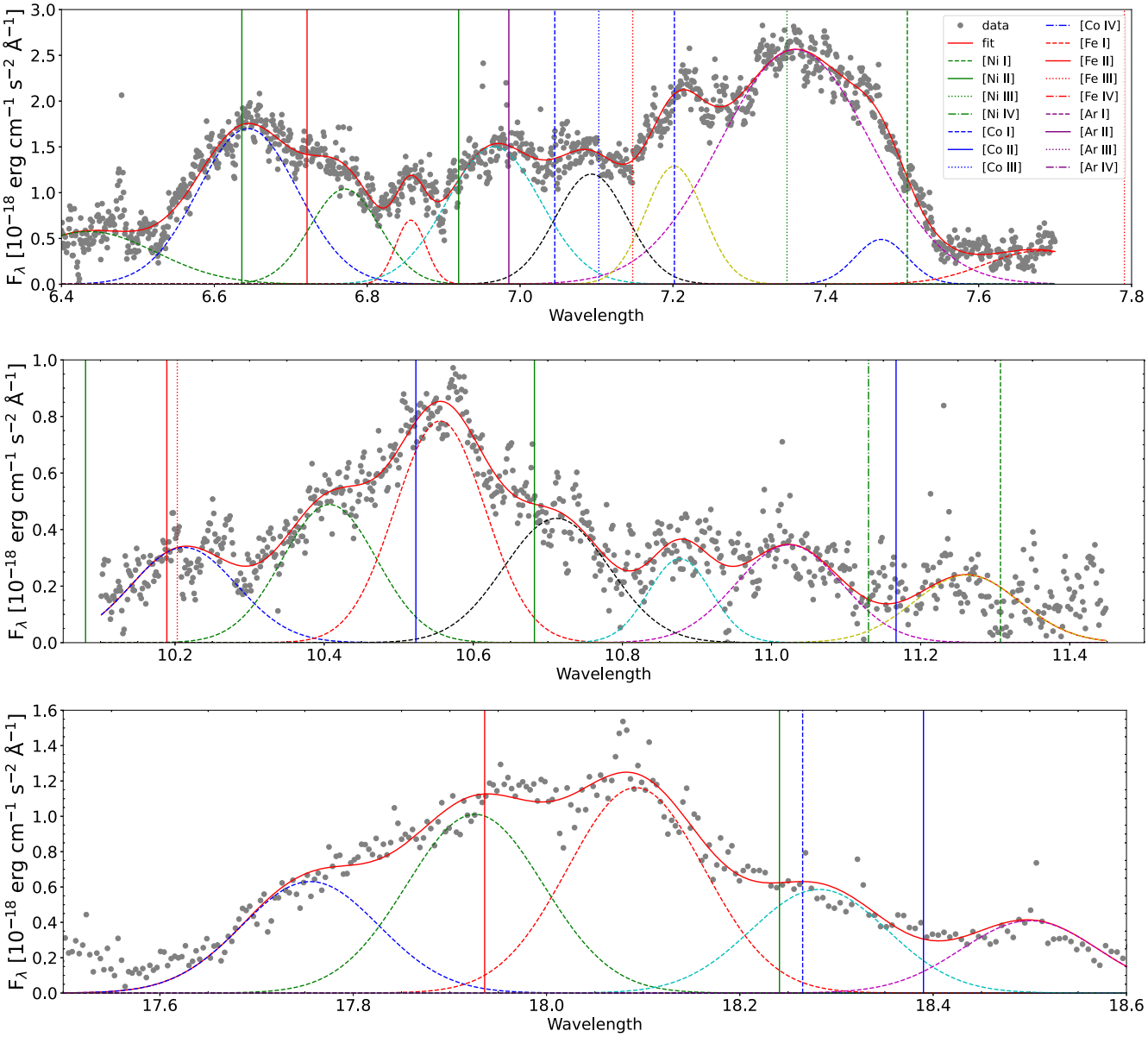

Figure C1. Spectral fits of three main regions in the data.

Table C1
The Best-fit Parameters from the Ions Used in Figure 10

Ion	Wavelength (μm)	v_{peak} (μm)	Error v_{peak} (F_λ)	Amplitude (F_λ)	Error Amplitude (μm)	σ (μm)	Error σ
[Ni II]	6.636	6.644	0.004	1.699	0.052	0.092	0.008
[Fe II]	6.721	6.771	0.005	1.040	0.109	0.064	0.008
[Ar II]	6.985	6.966	0.008	1.501	0.051	0.086	0.012
[Ni III]	7.349	7.360	0.005	2.564	0.024	0.139	0.013
[Co I]	7.202	7.202	0.004	1.288	0.167	0.054	0.005
[Co III]	7.103	7.093	0.006	1.203	0.152	0.066	0.012
[Co I]	7.507	7.472	0.003	0.489	0.195	0.048	0.011
[Fe II]	17.936	17.926	0.020	1.011	0.245	0.100	0.042
[Co I]	18.265	18.282	0.023	0.587	0.079	0.100	0.036
[Fe II]	10.189	10.212	0.011	0.337	0.019	0.100	0.016
[Co III]	10.523	10.555	0.010	0.784	0.162	0.085	0.023
[Co II]	10.682	10.712	0.027	0.439	0.059	0.100	0.040
[Co III]	11.888	11.917	0.002	1.013	0.008	0.196	0.002

of 18.6 μm due to the uncertainty in the channel 4 data; the fit around the [Co III] 11.888 μm feature is shown in the main body of the text (see Section 5.1).

Appendix D
Optical to 4.7 μm Line List from Models

For completeness, in Table D1, the line list from our models in the wavelength regime shorter than our observations is provided.

Table D1
Line Contributions to the Spectra from the Optical to 4.7 μm at +415 Days from the Reference Model with $\rho_c = 1.1 \times 10^9$ g cm^{-3} and $B = 10^6$ G

S	λ (μm)	Ion	S	λ (μm)	Ion	S	λ (μm)	Ion	S	λ (μm)	Ion	S	λ (μm)	Ion
	0.3689	[Co II]		0.4104	[Co II]		0.4116	[Fe II]		0.4178	[Fe II]	***	0.4245	[Fe II]
*	0.4246	[Fe II]	**	0.4278	[Fe II]	*	0.4289	[Fe II]		0.4307	[Fe II]	*	0.4321	[Fe II]
	0.4327	[Ni II]	*	0.4348	[Fe II]	*	0.4354	[Fe II]		0.436	[Fe II]		0.4361	[Fe II]
*	0.4374	[Fe II]		0.4415	[Fe II]	*	0.4418	[Fe II]		0.4453	[Fe II]	*	0.4459	[Fe II]
	0.4476	[Fe II]		0.449	[Fe II]		0.4494	[Fe II]		0.4501	[Co III]		0.4608	[Fe III]
	0.4624	[Co II]		0.4641	[Fe II]	***	0.4659	[Fe III]	*	0.4703	[Fe III]	*	0.4729	[Fe II]
*	0.4735	[Fe III]		0.4749	[Co II]	*	0.4756	[Fe III]	*	0.4771	[Fe III]		0.4804	[Co II]
*	0.4882	[Fe III]	*	0.4891	[Fe II]		0.4932	[Fe III]	**	0.5013	[Fe III]		0.5086	[Fe III]
*	0.5113	[Fe II]	**	0.516	[Fe II]		0.5222	[Fe II]	*	0.5263	[Fe II]		0.527	[Co II]
**	0.5272	[Fe III]		0.5298	[Fe II]	*	0.5335	[Fe II]	*	0.5378	[Fe II]		0.5414	[Fe III]
	0.5472	[Co II]		0.5548	[Co II]		0.5562	[Co II]		0.589	[Co III]		0.5976	[Fe I]
	0.6016	[Fe II]		0.6129	[Co III]		0.6197	[Co III]		0.6578	[Co III]		0.6586	[Co I]
	0.6669	[Ni II]		0.6855	[Fe II]		0.6934	[Co II]		0.7138	[Ar III]		0.7155	[Co III]
***	0.7157	[Fe II]	*	0.7174	[Fe II]		0.7249	[Co I]	***	0.7293	[Ca II]	**	0.7326	[Ca II]
*	0.738	[Ni II]	*	0.739	[Fe II]	*	0.7414	[Ni II]	**	0.7455	[Fe II]		0.7541	[Co II]
*	0.764	[Fe II]	*	0.7689	[Fe II]		0.7892	[Ni III]		0.803	[Co II]	**	0.8123	[Co II]
	0.8123	[Co II]		0.8303	[Ni II]		0.8336	[Co II]		0.8466	[Co II]		0.8469	[Co II]
	0.8502	[Ni III]		0.8546	[Co I]	*	0.8574	[Co II]		0.8583	[Co II]		0.8597	[Co I]
**	0.8619	[Fe II]	***	0.8894	[Fe II]	*	0.9036	[Fe II]	**	0.9054	[Fe II]		0.9071	[S III]
**	0.9229	[Fe II]	*	0.927	[Fe II]	*	0.9339	[Co II]	*	0.9345	[Co II]		0.9447	[Fe III]
	0.9474	[Fe II]		0.9533	[S III]		0.9642	[Co II]	*	0.9642	[Co II]		0.9697	[Co I]
	0.9705	[Fe III]		0.9983	[Fe II]	*	0.9483	[Fe II]	***	1.0191	[Co II]	*	1.0248	[Co II]
	1.0283	[Co II]		1.0283	[Co II]		1.0611	[Fe III]		1.0718	[Ni II]		1.0718	[Ni II]
**	1.0824	[S I]		1.0885	[Fe III]	*	1.0976	[Co II]		1.0994	[Si I]	*	1.1283	[Co II]
*	1.1309	[S I]		1.1616	[Ni II]		1.2122	[Fe II]		1.2525	[Fe II]	***	1.257	[Fe II]
**	1.2707	[Fe II]	*	1.2791	[Fe II]	*	1.2946	[Fe II]	*	1.2981	[Fe II]	**	1.3209	[Fe II]
*	1.321	[Fe I]	**	1.3281	[Fe II]		1.3422	[Fe I]		1.3556	[Fe I]		1.3676	[Fe I]
*	1.3722	[Fe II]	**	1.3733	[Fe I]		1.3762	[Fe I]		1.4055	[Co II]	**	1.4434	[Fe I]
	1.4972	[Co II]	***	1.5339	[Fe II]		1.5474	[Co II]		1.5488	[Co III]		1.5694	[Co II]
***	1.5999	[Fe II]		1.6073	[Si I]		1.6267	[Co II]	*	1.6347	[Co II]	***	1.644	[Fe II]
*	1.6459	[Si I]	***	1.6642	[Fe II]	**	1.6773	[Fe II]	*	1.7116	[Fe II]		1.7289	[Co II]
	1.7366	[Co II]		1.7413	[Co III]	**	1.7454	[Fe II]	**	1.7976	[Fe II]	**	1.8005	[Fe II]

Table D1
(Continued)

S	λ (μm)	Ion	S	λ (μm)	Ion	S	λ (μm)	Ion	S	λ (μm)	Ion	S	λ (μm)	Ion
*	1.8099	[Fe II]		1.8119	[Fe II]	*	1.904	[Co II]	**	1.9393	[Ni II]		1.9581	[Co III]
	2.0028	[Co III]		2.0073	[Fe II]		2.0418	[Ti II]	**	2.0466	[Fe II]		2.0492	[Ni II]
	2.0979	[Co III]		2.1334	[Fe II]	*	2.1457	[Fe III]		2.1605	[Ti II]	**	2.2187	[Fe III]
**	2.2425	[Fe III]	**	2.2443	[Fe II]		2.3086	[Ni II]	***	2.3486	[Fe III]		2.3695	[Ni II]
***	2.4781	[Fe II]	**	2.5255	[Co I]	*	2.6521	[Co I]	**	2.7173	[Fe III]	*	2.8713	[Co I]
**	2.8742	[Fe III]	**	2.9048	[Fe III]	**	2.9114	[Ni II]	*	2.9542	[Co I]	**	2,9610	[Fe II]
	3.0305	[Co I]	**	3.0439	[Fe III]		3.0457	[Co I]	***	3.12	[Ni I]		3.2294	[Fe III]
	3.3942	[Ni III]		3.4917	[Co III]	*	3.6334	[Co I]		3.7498	[Co I]		3.8023	[Ni III]
**	3.9524	[Ni I]	***	4.0763	[Fe II]		4.082	[Fe II]	**	4.115	[Fe II]		4.3071	[Co II]
	4.5196	[Ni I]	**	4.6077	[Fe II]									

Note. The relative strengths are indicated by the number of asterisks.

Appendix E
MIR Transitions without Cross Sections

Weak MIRI/MRS features are used to calibrate the atomic models. One of the main uncertainties in the modeling is the lack of atomic data for many weak transitions (Hoeflich et al. 2021) or, here, the lifetimes or Einstein coefficients $A_{l,u}$ for the spontaneous decay.

In principle, we follow the method employed by Kurucz (1993, 1995), who calibrated allowed cross sections by comparing synthetic spectra with the observed solar spectrum. Similarly, we make use of the MIRI spectrum of SN 2021aefx to estimate Einstein A values. We do not change the atomic models and only adjust atomic cross sections between known energy levels but without previously measured values. Because of the low densities and nonthermal excitation, the full rate equations are simulated for the given background.

However, the applicability of the method is limited by the S/N ≈ 5–10 in the continuum and the uncertainty in the absolute calibration between the channels (Section 6.3.2). Moreover, the features are smeared out over several 1000 km s^{-1}. Many weak features are present in the quasi-continuum in both the observations and synthetic spectra (see Figure 13), e.g., between 13 and 23 μm, but not always. Two features are predicted at 15.9 μm and 16.8 μm, whereas a single broad feature has been observed without a corresponding transition in Table E1 to fill the gap. The method can be made more complete by future SN Ia observations with MIRI/MRS during the early-time nebular phase. For SN 2021aefx at day +415, only a few features are well above the noise level and can be used individually. However, the underlying flux is produced by many weak lines of Fe, Co, and Ni I–IV and, at +415 days, a quasi-continuum of free–free and bound–free and some allowed lines produced in inner layers (Diamond et al. 2015). The A_{lu} values have been found by a Monte Carlo scheme for some individual transitions by attributing the "missing" continuum flux by a global default A_{lu} value, with the latter determined by the residual flux in the continuum around 9.5 ± 0.4 μm and 15 ± 2 μm. The values adopted are given in Tables E1 and E2. The corrections to the flux are on the percent level.

Table E1
Lifetimes of Transitions without Experimental Values Have Been Calculated Based on a Combination of Observations and the Base Model

λ (μm)	Ion	Term	$J_{l,u}$	A_{lu}	$E_{l,u}$ (cm^{-1})	λ (μm)	Ion	Term	$J_{l,u}$	A_{lu}	$E_{l,u}$ (cm^{-1})
5.022021	[Fe II]	a2G-a2P	7/2, 3/2	1E-3	16,369.41–18,360.64	5.051034	[Fe II]	b4P-b4F	5/2, 7/2	1E-3	20,830.55–22,810.35
5.022021	[Fe II]	a2G-a2P	7/2, 3/2	1E-3	16,369.41–18,360.64	5.051034	[Fe II]	b4P-b4F	5/2, 7/2	1E-3	20,830.55–22,810.35
5.0623456	[Fe II]	a6D-a4F	3/2, 5/2	1E-3	862.61–2837.98	5.105920	[Co II]	b1G-a3H	4, 6	1E-3	25,147.23–27,105.74
5.144614	[Fe II]	a2P-b4P	1/2, 5/2	1E-3	18,886.77–20,830.55	5.149301	[Co II]	a1D-a3P	2, 0	1E-3	11,651.28–13,593.29
5.157755	[Co II]	b3F-a3P	2, 2	1E-3	11,321.86–13,260.69	5.282999	[Fe II]	a2D2-b4P	5/2, 1/2	1E-3	20,516.95–22,409.82
5.301864	[Fe II]	a4G-a2F	11/2, 7/2	1E-3	25,428.79–27,314.92	5.3401693	[Fe II]	a6D-a4F	9/2, 9/2	1E-2	0.00–1872.60
5.3736547	[Fe II]	a6D-a4F	1/2, 5/2	1E-2	977.05–2837.98	5.396797	[Co II]	a3G-b3P	3, 1	1E-3	22,414.43–24,267.38
5.439462	[Co II]	b3F-a1D	4, 2	2E-3	9812.86–11,651.28	5.456068	[Fe II]	b2P-a2F	3/2, 5/2	1E-3	25,787.58–27,620.40
5.460209	[Fe II]	a2H-b4F	9/2, 9/2	1E-3	20,805.76–22,637.19	5.477981	[Fe I]	a5P-a3P	2, 1	1E-3	17,726.99–19,552.48
5.509410	[Fe II]	a4G-a2F	9/2, 5/2	1E-3	25,805.33–27,620.40	5.535132	[Fe II]	b4P-b4F	5/2, 9/2	1E-3	20,830.55–22,637.19
5.596278	[Co II]	b3P-c3P	2, 0	1E-3	24,074.42–25,861.32	5.604112	[Co II]	a3D-a3D	3, 1	1E-3	27,484.37–29,268.78
5.6316	[Co III]	a4P-a2G	5/2, 9/2	1E-3	15,201.90–16,977.60	5.6739070	[Fe II]	a6D-a4F	5/2, 7/2	1E-2	667.68–2430.14
5.801083	[Co II]	c3P-a1P	0, 1	1E-3	25,861.32–27,585.14	5.802874	[Fe II]	a2D2-b4F	3/2, 3/2	1E-3	21,308.00–23,031.28
5.826	[Co IV]	3H-3F2	6, 4	1E-3	23,679.50–25,396.00	5.845	[Ni IV]	4P-2G	5/2, 9/2	1E-3	18,118.60–19,829.60
5.868	[Co IV]	3H-3F2	5, 3	1E- 3	24,031.80–25,735.90	5.893	[Co IV]	3H-3F2	4, 2	1E-3	24,272.00–25,969.00
6.024136	[Co II]	a3G-b3P	3, 2	5E-3	22,414.43–24,074.42	6.102182	[Fe II]	a4G-a2F	7/2, 5/2	5E-3	25,981.65–27,620.40
6.129884	[Fe II]	a2D2-b4F	3/2, 5/2	5E-3	21,308.00–22,939.35	6.134290	[Fe II]	a2P-a2D2	1/2, 5/2	5E-3	18,886.77–20,516.95
6.153483	[Fe I]	a5P-a3P	1, 1	5E-3	17,927.38–19,552.48	6.227663	[Fe II]	a4H-a6S	7/2, 5/2	5E-3	21,711.90–23,317.64
6.260968	[Co II]	a3F-a3F	4, 2	3E-2	0.00–1597.20	6.332062	[Fe II]	b4P-b4P	5/2, 1/2	5E-3	20,830.55–22,409.82
6.3794832	[Fe II]	a6D-a4F	3/2, 7/2	2E-2	862.61–2430.14	6.389812	[Fe II]	a4G-a2F	5/2, 5/2	1E-3	26,055.41–27,620.40
6.547345	[Fe II]	b2P-a2F	3/2, 7/2	1E-3	25,787.58–27,314.92	6.624310	[Fe II]	a4G-a2F	9/2, 7/2	1E-3	25,805.33–27,314.92
6.626905	[Co II]	b3F-b3F	4, 2	2E-3	9812.86–11,321.86	6.62998	[Ni I]	3D-3D	3, 1	1E-2	204.79–1713.09
6.641916	[Fe II]	b4P-a6S	3/2, 5/2	1E-3	21,812.05–23,317.64	6.656252	[Fe II]	a2D2-b4F	3/2, 7/2	1E-3	21,308.00–22,810.35
6.721277	[Fe II]	a6D-a4F	7/2, 9/2	5E-2	384.79–1872.60	6.831	[Co IV]	3H-3F2	4, 3	1E-3	24,272.00–25,735.90
6.890	[Co III]	a4F-a4F	9/2, 5/2	1E-2	0.00–1451.30	6.986	[Ni IV]	4F-4F	7/2, 3/2	5E-3	1189.70–2621.10
7.201	[Co IV]	3P2-3H	2, 4	1E-3	22,883.30–24,272.00	7.217029	[Fe II]	a4H-b4F	13/2, 9/2	1E-3	21,251.58–22,637.19
7.246432	[Fe II]	a4H-b4F	11/2, 7/2	1E-3	21,430.36–22,810.35	7.290488	[Fe II]	a2H-a4H	11/2, 7/2	1E-3	20,340.25–21,711.90
7.330	[Co IV]	3H-3F2	5, 4	1E-3	24,031.80–25,396.00	7.48092	[Ni I]	3D-3F	2, 2	2E-2	879.82–2216.55
7.500338	[Fe II]	a4G-a2F	7/2, 7/2	1E-3	25,981.65–27,314.92	7.579280	[Fe II]	a4H-b4F	7/2, 3/2	1E-3	21,711.90–23,031.28
7.721459	[Fe II]	a2D2-b4P	5/2, 3/2	1E-3	20,516.95–21,812.05	7.888699	[Fe II]	b2H-a2F	9/2, 5/2	1E-3	26,352.77–27,620.40
7.939619	[Fe II]	a4G-a2F	5/2, 7/2	1E-3	26,055.41–27,314.92	8.055622	[Fe II]	a2H-a4H	11/2, 9/2	1E-3	20,340.25–21,581.62
8.066	[Co IV]	3P2-3F2	1, 2	1E-3	24,729.20–25,969.00	8.138479	[Fe II]	a4H-b4F	9/2, 7/2	1E-3	21,581.62–22,810.35
8.146939	[Fe II]	a4H-b4F	7/2, 5/2	1E-3	21,711.90–22,939.35	8.201847	[Fe II]	b4P-b4F	3/2, 3/2	1E-3	21,812.05–23,031.28
8.262448	[Co II]	a5F-a5F	5, 3	2E-3	3350.49–4560.79	8.286112	[Fe II]	a4H-b4F	11/2, 9/2	1E-3	21,430.36–22,637.19
8.299328	[Fe II]	a6D-a4F	5/2, 9/2	1E-3	667.68–1872.60	8.317945	[Co II]	a5P-a1G	3, 4	1E-3	17,771.51– 18,973.73
8.368601	[Fe II]	a2D2-a4H	5/2, 7/2	1E-3	20,516.95–21,711.90	8.37951	[Ni I]	3F-1D	2, 2	1E-3	2216.55–3409.94
8.735629	[Fe II]	b2H-a2F	11/2, 7/2	1E-3	26,170.18–27,314.92	8.87015	[Ni I]	3D-3F	3, 3	1E-2	204.79–1332.16
8.870707	[Fe II]	b4P-b4F	3/2, 5/2	1E-3	21,812.05–22,939.35	8.897	[Co IV]	3H-3F2	4, 4	1E-3	24,272.00–25,396.00
9.075902	[Fe II]	a2D2-b4P	3/2, 1/2	1E-3	21,308.00–22,409.82	9.103740	[Fe II]	a4H-b4F	7/2, 7/2	1E-3	21,711.90–22,810.35
9.173384	[Fe II]	a2H-a4H	11/2, 11/2	1E-3	20,340.25–21,430.36	9.279	[Co IV]	5D-5D	4, 2	1E-2	0.00–1077.70
9.321289	[Co II]	b3P-b1G	2, 4	1E-3	24,074.42–25,147.23	9.392655	[Fe II]	a2D2-a4H	5/2, 9/2	1E-3	20,516.95–21,581.62
9.473466	[Fe II]	a4H-b4F	9/2, 9/2	1E-3	21,581.62–22,637.19	9.522585	[Co II]	b3P-c3P	1, 1	1E-3	24,267.38–25,317.52
9.750	[Co III]	a4F-a4F	7/2, 3/2	1E-2	841.20–1866.80	9.933	[Co IV]	3P2-3F2	1, 3	1E-3	24,729.20–25,735.90
10.017024	[Fe II]	b4P-b4F	3/2, 7/2	1E-3	21,812.05–22,810.35	10.077445	[Fe I]	a3F-a3F	4, 2	1E-3	11,976.24–12,968.55
10.257231	[Co II]	c3P-c3P	2, 0	1E-3	24,886.40–25,861.32	10.358606	[Fe II]	a4F-a4F	9/2, 5/2	1E-3	1872.60–2837.98

Table E1
(Continued)

λ (μm)	Ion	Term	$J_{l,u}$	A_{lu}	$E_{l,u}$ (cm^{-1})	λ (μm)	Ion	Term	$J_{l,u}$	A_{lu}	$E_{l,u}$ (cm^{-1})
10.393377	[Fe II]	b2H-a2F	9/2, 7/2	1E-3	26,352.77–27,314.92	10.605061	[Co II]	b3F-a1D	3, 2	1E-3	10,708.33–11,651.28
10.612332	[Co II]	a5P-a1G	2, 4	1E-3	18,031.43–18,973.73	10.807321	[Fe II]	a4H-b4F	7/2, 9/2	1E-3	21,711.90–22,637.19
10.822771	[Fe II]	a4G-b2H	11/2, 9/2	1E-3	25,428.79–26,352.77	10.856891	[Co II]	a5F-a5F	4, 2	1E-3	4028.99–4950.06
10.972887	[Fe II]	a2H-a4H	11/2, 13/2	1E-3	20,340.25–21,251.58						

Note. The relative strengths of individual features are fitted. For many weak lines, a standard value has been assumed based on the overall spectra (see text).

Table E2
Same as Table 4 but for 11–30 μm

λ (μm)	Ion	Term	$J_{l,u}$	A_{lu}	$E_{l,u}$ (cm^{-1})	λ (μm)	Ion	Term	$J_{l,u}$	A_{lu}	$E_{l,u}$ (cm^{-1})
11.015432	[Fe II]	b4P-a6S	1/2, 5/2	1E-3	22,409.82–23,317.64	11.035906	[Fe II]	a2H-a4H	9/2, 7/2	1E-3	20,805.76–21,711.90
11.037065	[Co II]	b3P-c3P	0, 1	1E-3	24,411.48–25,317.52	11.36601	[Ni I]	3F-3D	4, 2	2E-2	0.00–879.82
11.398313	[Fe II]	a4G-b2P	5/2, 1/2	1E-3	26,055.41–26,932.73	11.825	[Co IV]	3G-3G	5, 3	1E-3	29,021.80–29,867.50
11.908	[Ni IV]	4P-4P	5/2, 1/2	1E-3	18,118.60–18,958.40	12.077222	[Fe I]	a5P-a3P	3, 2	1E-3	17,550.18–18,378.19
12.315574	[Co II]	b3P-c3P	2, 2	1E-3	24,074.42–24,886.40	12.503266	[Fe I]	a5F-a5F	5, 3	2E-3	6928.27–7728.06
12.55624	[Co II]	a3H-a3H	6, 4	1E-3	27,105.74–27,902.16	12.659782	[Co II]	a3G-a3G	5, 3	1E-3	21,624.53–22,414.43
12.889058	[Fe II]	a2H-a4H	9/2, 9/2	1E-3	20,805.76–21,581.62	13.314485	[Fe II]	b4P-a4H	5/2, 9/2	1E-3	20,830.55–21,581.62
13.48815	[Fe II]	a4G-b2H	11/2, 11/2	1E-3	25,428.79–26,170.18	13.790212	[Fe II]	a4D-a4D	7/2, 3/2	1E-3	7955.32–8680.47
13.924	[Co IV]	5D-5D	3, 1	1E-2	639.10–1357.30	14.204404	[Fe I]	a5D-a5D	4, 2	1E-2	0.00–704.01
14.54189	[Fe II]	b2P-a2F	1/2, 5/2	1E-3	26,932.73–27,620.40	14.548612	[Fe II]	a4F-a4F	7/2, 3/2	5E-3	2430.14–3117.49
14.69637	[Fe II]	b4F-a6S	9/2, 5/2	1E-3	22,637.19–23,317.64	14.977170	[Fe II]	a6D-a6D	9/2, 5/2	1E-2	0.00–667.68
15.35631	[Fe I]	a5P-a3P	2, 2	1E-3	17,726.99–18,378.19	15.53014	[Co II]	a5F-a5F	3, 1	1E-3	4560.79–5204.70
16.01042	[Fe II]	a2H-a4H	9/2, 11/2	1E-3	20,805.76–21,430.36	16.09101	[Fe II]	b4P-b4F	1/2, 3/2	1E-3	22,409.82–23,031.28
16.407	[Co III]	a4P-a4P	5/2, 1/2	1E-3	15,201.90–15,811.40	16.41982	[Fe I]	a5F-a5F	4, 2	5E-3	7376.76–7985.78
16.878	[Co IV]	3H-3H	6, 4	1E- 3	23,679.50–24,272.00	17.572	[Ni III]	3P-3P	2, 0	1E-3	16,661.60– 17,230.70
17.63255	[Co II]	a5P-a5P	3, 1	1E-3	17,771.51–18,338.64	18.08790	[Fe II]	a4G-a4G	11/2, 7/2	1E-3	25,428.79–25,981.65
18.26684	[Fe II]	a4G-b2H	9/2, 9/2	1E-3	25,805.33–26,352.77	18.88455	[Fe II]	b4P-b4F	1/2, 5/2	1E-3	22,409.82–22,939.35
19.71262	[Fe II]	b4F-a6S	7/2, 5/2	1E-3	22,810.35–23,317.64	19.83944	[Fe II]	a2D2-b4P	3/2, 3/2	1E-3	21,308.00–21,812.05
19.8624	[Ni I]	3D-3F	1, 2	2E-3	1713.09– 2216.55	20.928182	[Fe II]	a6D-a6D	7/2, 3/2	3E-3	384.79–862.61
20.94479	[Fe II]	b4P-a2D2	5/2, 3/2	3E-3	20,830.55–21,308.00	21.05613	[Co II]	b3P-c3P	0, 2	2E-3	24,411.48–24,886.40
21.17751	[Fe I]	a5D-a5D	3, 1	2E-3	415.93–888.13	22.1069	[Ni I]	3D-3F	2, 3	1E-2	879.82–1332.16
22.18259	[Fe I]	a5P-a3P	1, 2	1E-3	17,927.38–18,378.19	22.43057	[Fe II]	a2H-a4H	9/2, 13/2	2E-3	20,805.76–21,251.58
23.23350	[Fe II]	a4P-a4P	5/2, 1/2	2E-3	13,474.45–13,904.86	23.43820	[Fe I]	a5F-a5F	3, 1	2E-3	7728.06–8154.71
23.93558	[Co II]	a3D-a3H	3, 4	2E-3	27,484.37–27,902.16	24.04	[Co IV]	5D-5D	2, 0	1E-2	1077.70–1493.60
24.5422	[Ni I]	3P-3P	2, 0	1E-3	15,609.84–16,017.31	24.75877	[Fe II]	a2D2-a4H	3/2, 7/2	1E-3	21,308.00–21,711.90
26.2520	[Ni I]	3F-3D	3, 1	2E-3	1332.16–1713.09	26.43517	[Fe II]	b4F-a6S	5/2, 5/2	1E-3	22,939.35–23,317.64
26.51106	[Fe I]	a5P-a5P	3, 1	1E-3	17,550.18–17,927.38	26.63	[Co III]	a2D2-a2H	5/2, 9/2	1E-3	23,058.80–23,434.30
26.94532	[Fe II]	a4G-b2H	7/2, 9/2	1E-3	25,981.65–26,352.77	27.40822	[Fe II]	a4G-b2H	9/2, 11/2	1E-3	25,805.33–26,170.18

Note. The relative strengths of individual features are fitted. For many weak lines, a standard value has been assumed based on the overall spectra (see text).

ORCID iDs

C. Ashall https://orcid.org/0000-0002-5221-7557
P. Hoeflich https://orcid.org/0000-0002-4338-6586
E. Baron https://orcid.org/0000-0001-5393-1608
M. Shahbandeh https://orcid.org/0000-0002-9301-5302
J. M. DerKacy https://orcid.org/0000-0002-7566-6080
K. Medler https://orcid.org/0000-0001-7186-105X
B. J. Shappee https://orcid.org/0000-0003-4631-1149
M. A. Tucker https://orcid.org/0000-0002-2471-8442
E. Fereidouni https://orcid.org/0009-0001-9148-8421
T. Mera https://orcid.org/0000-0001-5888-2542
J. Andrews https://orcid.org/0000-0003-0123-0062
D. Baade https://orcid.org/0000-0003-1637-9679
K. A. Bostroem https://orcid.org/0000-0002-4924-444X
P. J. Brown https://orcid.org/0000-0001-6272-5507
C. R. Burns https://orcid.org/0000-0003-4625-6629
A. Burrow https://orcid.org/0000-0002-5380-0816
A. Cikota https://orcid.org/0000-0001-7101-9831
T. de Jaeger https://orcid.org/0000-0001-6069-1139
A. Do https://orcid.org/0000-0003-3429-7845
Y. Dong https://orcid.org/0000-0002-7937-6371
I. Dominguez https://orcid.org/0000-0002-3827-4731
O. Fox https://orcid.org/0000-0003-2238-1572
L. Galbany https://orcid.org/0000-0002-1296-6887
E. Y. Hsiao https://orcid.org/0000-0003-1039-2928
K. Krisciunas https://orcid.org/0000-0002-6650-694X
B. Khaghani https://orcid.org/0009-0005-0311-0058
S. Kumar https://orcid.org/0000-0001-8367-7591
J. Lu https://orcid.org/0000-0002-3900-1452
J. R. Maund https://orcid.org/0000-0003-0733-7215
P. Mazzali https://orcid.org/0000-0001-6876-8284
N. Morrell https://orcid.org/0000-0003-2535-3091
F. Patat https://orcid.org/0000-0002-0537-3573
C. Pfeffer https://orcid.org/0000-0002-7305-8321
M. M. Phillips https://orcid.org/0000-0003-2734-0796
J. Schmidt https://orcid.org/0000-0002-2617-5517
S. Stangl https://orcid.org/0000-0001-5570-6666
C. P. Stevens https://orcid.org/0000-0003-0763-6004
M. D. Stritzinger https://orcid.org/0000-0002-5571-1833
N. B. Suntzeff https://orcid.org/0000-0002-8102-181X
C. M. Telesco https://orcid.org/0000-0002-0036-9292
L. Wang https://orcid.org/0000-0001-7092-9374
Y. Yang https://orcid.org/0000-0002-6535-8500

References

Alsabti, A. W., & Murdin, P. 2017, Handbook of Supernovae (Berlin: Springer)
Argyriou, I., Glasse, A., Law, D. R., et al. 2023, A&A, 675, A111
Ashall, C., Baron, E., Hoeflich, P. A., et al. 2021, MIR Spectroscopy of Type Ia Supernovae: The Key to Unlocking their Explosions and Element Production, JWST Proposal, Cycle 1, #2114
Ashall, C., Lu, J., Shappee, B. J., et al. 2022, ApJL, 932, L2
Ashall, C., Mazzali, P. A., Pian, E., & James, P. A. 2016, MNRAS, 463, 1891
Astropy Collaboration, Price-Whelan, A. M., Lim, P. L., et al. 2022, ApJ, 935, 167
Astropy Collaboration, Price-Whelan, A. M., Sipőcz, B. M., et al. 2018, AJ, 156, 123
Astropy Collaboration, Robitaille, T. P., Tollerud, E. J., et al. 2013, A&A, 558, A33
Axelrod, T. S. 1980, PhD thesis, Univ. of California, Santa Cruz
Berger, M. B., Hubbell, J. H., Seltzer, S., Coursey, J., & Zucker, D. 1998, NIST Standard Reference Database 8 (XGAM) 87-3597, NIST, doi:10.18434/T48G6X
Blondin, S., Dessart, L., Hillier, D. J., Ramsbottom, C. A., & Storey, P. J. 2023, A&A, 678, A170
Boos, S. J., Townsley, D. M., Shen, K. J., Caldwell, S., & Miles, B. J. 2021, ApJ, 919, 126
Brachwitz, F., Dean, D. J., Hix, W. R., et al. 2000, ApJ, 536, 934
Burrow, A., Baron, E., Ashall, C., et al. 2020, ApJ, 901, 154
Bushouse, H., Eisenhamer, J., Dencheva, N., et al. 2023, JWST Calibration Pipeline v1.9.4, Zenodo, doi:10.5281/zenodo.7577320
Chen, N. M., Tucker, M. A., Hoyer, N., et al. 2023, ApJL, 944, L28
Chen, N. M., Tucker, M. A., Hoyer, N., et al. 2023, ApJL, 944, L28
Childress, M. J., Hillier, D. J., Seitenzahl, I., et al. 2015, MNRAS, 454, 3816
Cikota, A., Patat, F., Wang, L., et al. 2019, MNRAS, 490, 578
DerKacy, J. M., Ashall, C., Hoeflich, P., et al. 2023a, ApJL, 945, L2
DerKacy, J. M., Baron, E., Hoeflich, P. A., et al. 2023b, Examining the Heart of Type Ia Supernova 2021aefx with Ultra-Late Time Spectra, JWST Proposal, Cycle 2, #3726
DerKacy, J. M., Ashall, C., Hoeflich, P., et al. 2024a, ApJ, 961, 187
DerKacy, J. M., Baron, E., Hoeflich, P. A., et al. 2024b, Examining the Heart of Type Ia Supernova 2021aefx with Ultra-Late Time Spectra, JWST Proposal, Cycle 3, #6582
Diamond, T. R., Hoeflich, P., & Gerardy, C. L. 2015, ApJ, 806, 107
Diamond, T. R., Hoeflich, P., Hsiao, E. Y., et al. 2018, ApJ, 861, 119
Domínguez, I., Höflich, P., & Straniero, O. 2001, ApJ, 557, 279
Elagali, A., Staveley-Smith, L., Rhee, J., et al. 2019, MNRAS, 487, 2797
Fesen, R. A., Höflich, P. A., & Hamilton, A. J. S. 2015, ApJ, 804, 140
Fink, M., Kromer, M., Seitenzahl, I. R., et al. 2014, MNRAS, 438, 1762
Fisher, R., & Jumper, K. 2015, ApJ, 805, 150
Fransson, C., & Jerkstrand, A. 2015, ApJL, 814, L2
Galbany, L., Ashall, C., Höflich, P., et al. 2019, A&A, 630, A76
Gamezo, V. N., Khokhlov, A. M., & Oran, E. S. 2005, ApJ, 623, 337
Gamezo, V. N., Khokhlov, A. M., Oran, E. S., Chtchelkanova, A. Y., & Rosenberg, R. O. 2003, Sci, 299, 77
Gerardy, C. L., Meikle, W. P. S., Kotak, R., et al. 2007, ApJ, 661, 995
Gronow, S., Côté, B., Lach, F., et al. 2021, A&A, 656, A94
Haensel, P. 1995, SSRv, 74, 427
Harris, C. R., Millman, K. J., van der Walt, S. J., et al. 2020, Natur, 585, 357
Hoeflich, P. 2002, arXiv:astro-ph/0207103
Hoeflich, P. 2017, in Handbook of Supernovae, ed. A. W. Alsabti & P. Murdin (Berlin: Springer), 1151
Hoeflich, P., Khokhlov, A. M., & Wheeler, J. C. 1995, ApJ, 444, 831
Hoeflich, P., Hsiao, E. Y., Ashall, C., et al. 2017, ApJ, 846, 58
Hoeflich, P., Ashall, C., Fisher, A., et al. 2019, Nuclei in the Cosmos XV (Berlin: Springer), 187
Hoeflich, P., Ashall, C., Bose, S., et al. 2021, ApJ, 922, 186
Hoeflich, P., Yang, Y., Baade, D., et al. 2023, MNRAS, 520, 560
Höflich, P. 2003a, in ASP Conf. Ser. 288, Stellar Atmosphere Modeling, ed. I. Hubeny, D. Mihalas, & K. Werner (San Francisco, CA: ASP), 371
Höflich, P. 2003b, in ASP Conf. Ser. 288, Stellar Atmosphere Modeling, ed. I. Hubeny, D. Mihalas, & K. Werner (San Francisco, CA: ASP), 185
Höflich, P. 2006, NuPhA, 777, 579
Höflich, P. 2009, in AIP Conf. Ser. 1171, Recent Directions in Astrophysical Quantitative Spectroscopy and Radiation Hydrodynamics, ed. I. Hubeny (Melville, NY: AIP), 161
Höflich, P., Gerardy, C. L., Marion, H., & Quimby, R. 2006, NewAR, 50, 470
Höflich, P., Gerardy, C. L., Nomoto, K., et al. 2004, ApJ, 617, 1258
Höflich, P., & Stein, J. 2002, ApJ, 568, 779
Hosseinzadeh, G., Sand, D. J., Lundqvist, P., et al. 2022, ApJL, 933, L45
Hoyle, F., & Fowler, W. A. 1960, ApJ, 132, 565
Hristov, B., Collins, D. C., Hoeflich, P., Weatherford, C. A., & Diamond, T. R. 2018, ApJ, 858, 13
Hristov, B., Hoeflich, P., & Collins, D. C. 2021, ApJ, 923, 210
Hunter, J. D. 2007, CSE, 9, 90
Iben, I. J., & Tutukov, A. V. 1984, ApJS, 54, 335
JDADF Developers, Averbukh, J., Bradley, L., et al. 2023, Jdaviz v3.2.1, Zenodo, doi:10.5281/zenodo.7600492
Jerkstrand, A., Maeda, K., & Kawabata, K. S. 2020, Sci, 367, 415
Khokhlov, A. M. 1991, A&A, 245, 114
Khokhlov, A. M. 2000, arXiv:astro-ph/0008463
Kozma, C., & Fransson, C. 1992, ApJ, 390, 602
Kumar, S., Hsiao, E. Y., Ashall, C., et al. 2023, ApJ, 945, 27
Kurucz, R. L. 1993, PhST, 47, 110
Kurucz, R. L. 1995, HiA, 10, 579
Kwok, L. A., Siebert, M. R., Johansson, J., et al. 2024, ApJ, 966, 135
Kwok, L. A., Jha, S. W., Temim, T., et al. 2023, ApJL, 944, L3
Langanke, K., & Martínez-Pinedo, G. 2000, NuPhA, 673, 481
Livne, E. 1999, ApJL, 527, L97

Livne, E., & Arnett, D. 1995, ApJ, 452, 62
Maguire, K., Sim, S. A., Shingles, L., et al. 2018, MNRAS, 477, 3567
Marietta, E., Burrows, A., & Fryxell, B. 2000, ApJS, 128, 615
Mayker Chen, N., Tucker, M. A., Hoyer, N., et al. 2023, ApJL, 944, L28
Mazzali, P. A., Röpke, F. K., Benetti, S., & Hillebrandt, W. 2007, Sci, 315, 825
Mazzali, P. A., Bikmaev, I., Sunyaev, R., et al. 2020, MNRAS, 494, 2809
McClelland, C. M., Garnavich, P. M., Milne, P. A., Shappee, B. J., & Pogge, R. W. 2013, ApJ, 767, 119
Mera Evans, T. B., Hoeflich, P., & Diehl, R. 2022, ApJ, 930, 107
Motohara, K., Maeda, K., Gerardy, C. L., et al. 2006, ApJL, 652, L101
Ni, Y. Q., Moon, D.-S., Drout, M. R., et al. 2023, ApJ, 959, 132
Ni, Y. Q., Moon, D.-S., Drout, M. R., et al. 2023, ApJ, 959, 132
Nomoto, K. 1982, ApJ, 253, 798
Pakmor, R., Seitenzahl, I. R., Ruiter, A. J., et al. 2024, A&A, 686, A227
Pakmor, R., Seitenzahl, I. R., Ruiter, A. J., et al. 2024, A&A, 686, A227
Patat, F., Höflich, P., Baade, D., et al. 2012, A&A, 545, A7
Pejcha, O., Antognini, J. M., Shappee, B. J., & Thompson, T. A. 2013, MNRAS, 435, 943
Penney, R., & Hoeflich, P. 2014, ApJ, 795, 84
Poludnenko, A. Y., Chambers, J., Ahmed, K., Gamezo, V. N., & Taylor, B. D. 2019, Sci, 366, aau7365
Remming, I. S., & Khokhlov, A. M. 2014, ApJ, 794, 87
Riess, A. G. 2017, in Handbook of Supernovae, ed. A. W. Alsabti & P. Murdin (Berlin: Springer), 2615
Roy, N. C., Tiwari, V., Bobrick, A., et al. 2022, ApJL, 932, L24
Seitenzahl, I. R., & Townsley, D. M. 2017, in Handbook of Supernovae, ed. A. W. Alsabti & P. Murdin (Berlin: Springer), 1955
Shahbandeh, M., Ashall, C., Hoeflich, P., et al. 2024, arXiv:2401.14474
Shen, K. J., Kasen, D., Miles, B. J., & Townsley, D. M. 2018, ApJ, 854, 52
Shingles, L. J., Sim, S. A., Kromer, M., et al. 2020, MNRAS, 492 2029
Siebert, M. R., Kwok, L. A., Johansson, J., et al. 2024, ApJ, 960, 88
Sugimoto, D., Fujimoto, M. Y., Nariai, K., & Nomoto, K. 1979, in IAU Symp. 53, White Dwarfs and Variable Degenerate Stars, ed. H. M. van Horn, V. Weidemann, & M. P. Savedoff, 280
Tartaglia, L., Sand, D. J., Valenti, S., et al. 2018, ApJ, 853, 62
Telesco, C. M., Höflich, P., Li, D., et al. 2015, ApJ, 798, 93
Thielemann, F.-K. 2019, in Nuclei in the Cosmos XV, ed. A. Formicola (Berlin: Springer), 125
Thompson, T. A. 2011, ApJ, 741, 82
Tucker, M. A., Ashall, C., Shappee, B. J., et al. 2022, ApJL, 926, L25
van Hoof, P. A. M. 2018, Galax, 6, 63
Virtanen, P., Gommers, R., Oliphant, T. E., et al. 2020, NatMe, 17, 261
Webbink, R. F. 1984, ApJ, 277, 355
Whelan, J., & Iben, Icko, J. 1973, ApJ, 186, 1007
Wilk, K. D., Hillier, D. J., & Dessart, L. 2018, MNRAS, 474, 3187
Yang, Y., Hoeflich, P., Baade, D., et al. 2020, ApJ, 902, 46
Yang, Y., Yan, H., Wang, L., et al. 2022, ApJ, 939, 18